(NASA-CR-161769) THEORETICAL INVESTIGATION OF THE GENERATION AND INJECTION OF ELECTROMAGNETIC WAVES IN SPACE PLASMA BY MEANS OF A LONG-ORBITING TETHER Final Report, 11 Dec. (Smithsonian Astrophysical G3/32 42451

N81-24322

Unclas

THEORETICAL INVESTIGATION OF THE GENERATION AND INJECTION OF ELECTROMAGNETIC WAVES IN SPACE PLASMA BY MEANS OF A LONG-ORBITING TETHER

NASA Contract NAS8-33520

For the period 11 December 1979 through 10 December 1980

Final Report

Principal Investigator
Dr. Mario D. Grossi

Prepared for

National Aeronautics and Space Administration
George C. Marshall Space Flight Center
Marshall Space Flight Center, Alabama 35812

February 1981

Smithsonian Institution
Astrophysical Observatory
Cambridge, Massachusetts 02138

The Smithsonian Astrophysical Observatory
and the Harvard College Observatory
are members of the
Center for Astrophysics

The NASA Technical Officer for this contract was Dr. William B. Johnson
Space Sciences Laboratory, NASA, Marshall Space Flight Center, Alabama 35812

THEORETICAL INVESTIGATION OF THE GENERATION AND INJECTION OF ELECTROMAGNETIC WAVES IN SPACE PLASMA BY MEANS OF A LONG-ORBITING TETHER

NASA Contract NAS8-33520

For the period 11 December 1979 through 10 December 1980

Final Report

Principal Investigator
Dr. Mario D. Grossi

Prepared for

National Aeronautics and Space Administration
George C. Marshall Space Flight Center
Marshall Space Flight Center, Alabama 35812

February 1981

Smithsonian Institution
Astrophysical Observatory
Cambridge, Massachusetts 02138

The Smithsonian Astrophysical Observatory
and the Harvard College Observatory
are members of the
Center for Astrophysics

The NASA Technical Officer for this contract was Dr. William G. Johnson
Space Sciences Laboratory, NASA, Marshall Space Flight Center, Alabama 35812

Acknowledgement

The author of this Report is Dr. Marino Dobrowolny, Visiting Scientist at SAO from Laboratorio Plasma Spazio, C.N.R., Frascati, Italy.

During his stay at SAO in 1980, Dr. M. Dobrowolny was supported in part by Contract NAS8-33520, in part by Laboratorio Plasma Spazio, C.N.R.

Foreword

This Final Report fulfills the obligations of the Smithsonian Astrophysical Observatory (SAO) on Contract NAS8-33520 received from NASA, Marshall Space Flight Center (NASA-MSFC).

The NASA Technical Officer for this Contract was Dr. William G. Johnson, Code ES01, Space Sciences Laboratory, NASA-MSFC, Marshall Space Flight Center, Alabama, 35812. At SAO, Dr. Mario D. Grossi was the Principal Investigator and Mr. Richard S. Taylor the Program Manager.

This Final Report illustrates the results accomplished during the period of contract performance: January 1, 1980 to December 31, 1980.

Abstract

An analysis of the various mechanisms of electromagnetic wave generation by the Shuttle-borne orbiting tether of the T.S.S. Facility has shown that significant electrodynamic power levels are available even when overestimating the loss mechanisms expected to intervene. For instance, with the tether deployed downwards, electrodynamic power levels of a few kilowatts are generated, when the radius of the terminating balloon is 5 meters or larger. For tethers deployed upwards (and when an electron gun onboard the Shuttle keeps it at plasma potential) electrodynamic power levels of 10 kilowatts are available, for balloon radii as small as 2 meters.

This electrodynamic power is in part dissipated by Joule losses in the tether, in part goes to accelerate electrons through the sheath surrounding the balloon (when in a downward deployment), and in part goes into e.m. wave generation. The Alfven Wings are the most interesting wave generation mechanism that is activated by the orbiting tether, although from the standpoint of practical applications, the use of the tether as a driven antenna, by pulsing its DC current, appears the most promising one. A preliminary estimate shows that a 100 km tether in orbit would produce ULF/ELF signals that are detectable on the ground with state-of-the-art magnetometric instrumentation.

The power that is expected to go into the acceleration of secondary electrons produces effects that range from the excitation of e.m. instabilities and consequent e.m. emissions at the gyrofrequency (emissions that are reputed to be at a low power level), to the excitation of luminous phenomena, extending into the UV band by the bombardment of upper atmospheric layers by the accelerated electrons.

High-priority topics that require further study are the point above of the excitation of instabilities and generation of luminous emissions by accelerated electrons, as well as the generation of ULF/ELF waves by using the tether as a driven antenna.

Table of Contents

Table of Contents (Continued)

List of Illustrations

List of Illustrations (continued)

Page

List of Tables

List of Symbols

v	velocity
v_o	Shuttle velocity
km	kilometer
sec	second
L	length
r_w	wire radius
E	electric field, V/m
B	magnetic field intensity, gauss
V	voltage, electric field potential
f_{ce}	electron cyclotron frequency
f_{pe}	electron plasma frequency
I	current modulus (absolute value)
i_s	current (at Shuttle end)
i_B	current (at balloon end)
V_s	Shuttle potential
V_B	balloon potential
j	species (i = ions, e = electrons)
i_j	contribution of species j to current
i_{jo}	as above, at station 0
$i_{\ell o}$	contribution of electron to current, at station 0
i_{io}	contribution to ions to current, at station 0
n_ℓ	electron density
v_{th}	thermal velocity
T_e	electron temperature

(List of Symbols) (continued)

e	electron charge
λ_{de}	Debye length
R_B	radius of balloon
R	electrode radius
K	Boltzman constant
f	function of ----
ϕ^*	abscissa of graph in Figure 2
ρ	resistivity of wire ($\mu\Omega m$)
R_W	total resistance of wire, ohm
$\Delta\phi_o$	electromotive force
$R_W i$	ohmic potential drop (ohmic law) in the wire
$i(R_B)$	current when balloon radius is R_B
R_{sh} or R_{sheat}	thickness of plasma sheath
m_i	mass of ion
h	height above see level
R_i	Larmor radius for ion
R_e	Larmor radius for electrons
α	parameter (introduced by equation 2.14)
$i^{(e)}$	contribution to current of the electrons, taking secondary emission from balloon into account
$i^{(i)}$	contribution to current of the ion, as above
$\delta(\lvert V_B \rvert)$	secondary emission yield as a function of balloon potential
γ_i	electron yields (Figure 11) of various ions
P_1	primary electrodynamic power
P_2	power lost in wire's ohmic (Joule) losses

List of Symbols (Continued)

P_4	power available for excitation of wave processes outside tether
P_3	power absorbed by the process of accelerating electrons
i_{sec}	current in secondary electrons
R_r	external radius of sheath region ($R_r = R_B + R_{sh}$)
$\alpha^{(e)}$	parameter (introduced by equation 3.3)
$v_{\parallel o}$	"parallel" electron velocity at the exit of sheath region
$v_{\perp o}$	"perpendicular" electron velocity, at the exit of sheath region
E_{R_r}	electric field at the edge of the sheath region
ρ_1	distance from $\underline{B}$ axis in Figure 20 ($\rho_1 = R_r \sin\theta$)
θ	angle between R_r and $\underline{B}$, in Figure 20
$n_b(\rho_1)$	density of secondary electrons, as a function of ρ_1
y	arctan $\frac{v_{\parallel o}}{v_{\perp o}}$ (introduced by equation 3.9)
n	index of refraction ($n = \frac{kc}{\omega}$)
ω	$= 2\pi f$
k	wave number
ν	integer (positive, negative or zero)
ω_{pe}	$= 2\pi f_{pe}$
Ω_{ce}	$= 2\pi f_{ce}$
PD	power density
kR	kiloroengten
Λ_{ij}	rank 2 tensor (i,j = 1,2,3)

List of Symbols (Continued)

$\underline{J}^o$	current density
x_i, x_j	$x_{i,i} = \frac{k_{i,j}}{\lvert k \rvert}$
ε_{ij}	dielectric tensor, magnetized plasma
δ_{ij}	kroneker symbol
δ	Dirac delta function
dy	conductor's dimension in direction of motion
ω^*	$= \frac{v_o}{dy}$
μ_o	permettivity of free space
ρ_p	plasma mass density
v_A	Alfven velocity
I_{AW}	current in the wire due to Alfvenic disturbance
θ_A	arctan $\frac{v_o}{v_A}$
i_R	upper limit of current in wire, set by wire resistance
I_c	current in the wire due to particle collection
$\mathcal{R}$	reflection coefficient
χ	$\chi = \frac{\Sigma p}{\Sigma_{AW}}$ (equation 4.30)
Σp	Pedersen integrated conductivity
Σ_{AW}	Alfven wave conductivity
τ	Alfven wave round-trip time
$\frac{1}{e}$	$\frac{1}{2.71828}$
Δy	distance that the tether moves during τ
v_g	wave group velocity

List of Symbols (Continued)

P_{AW}	power of Alfven wave
W	wave volumetric energy density
TSS	Tethered Satellite System
α	angle between velocity and magnetic field
Z_{AW}	wave impedence of Alfven waves
U	radiation intensity (power for unit solid angle)
$d\Omega$	a spreading factor quantity
d_{AE}	another spreading factor quantity
μ	index of refraction in ionosphere ($\mu = \frac{c}{v}$)
At	Ampere turn

1. Introduction

1.1 Rationale of the Investigation

The theoretical investigation illustrated in this report concerns the generation and injection of electromagnetic waves in space plasma by means of a long-orbiting tether moving in the ionosphere.

This is a general subject, since there are several electrodynamic phenomena associated with the moving tether and, correspondingly, a number of problems to be tackled. Before entering a quantitative study for any of these phenomena, it is necessary first to have a physical understanding of them, and second, to be able to estimate their relative importance. These are in fact the basic purposes of this report. The study concludes with a discussion of which phenomena are worth deeper study in view of an observational program using the Shuttle-based TSS facility.

1.2 The Various Mechanisms of Electrodynamic Interaction and Generation of Electromagnetic Waves

The configuration that we will study involves a metallic tether connected to the Shuttle at one end, and to a conducting balloon at the other. The tether can be deployed both upward and downward with respect to the Shuttle, which amounts, from the electrodynamic point of view, to exchanging the polarity of two end electrodes (the balloon and the conducting part of the Shuttle) with respect to the plasma, as indicated in Figure 1.

The results we will report refer primarily to a tether moving perpendicularly to magnetic field lines, at the Shuttle velocity:

$$V = 7.8 \text{ km/sec}$$

Length and radius of the tether are taken as:

$$L = 100 \text{ km}, \ r_W = 0.5 \text{ mm}$$

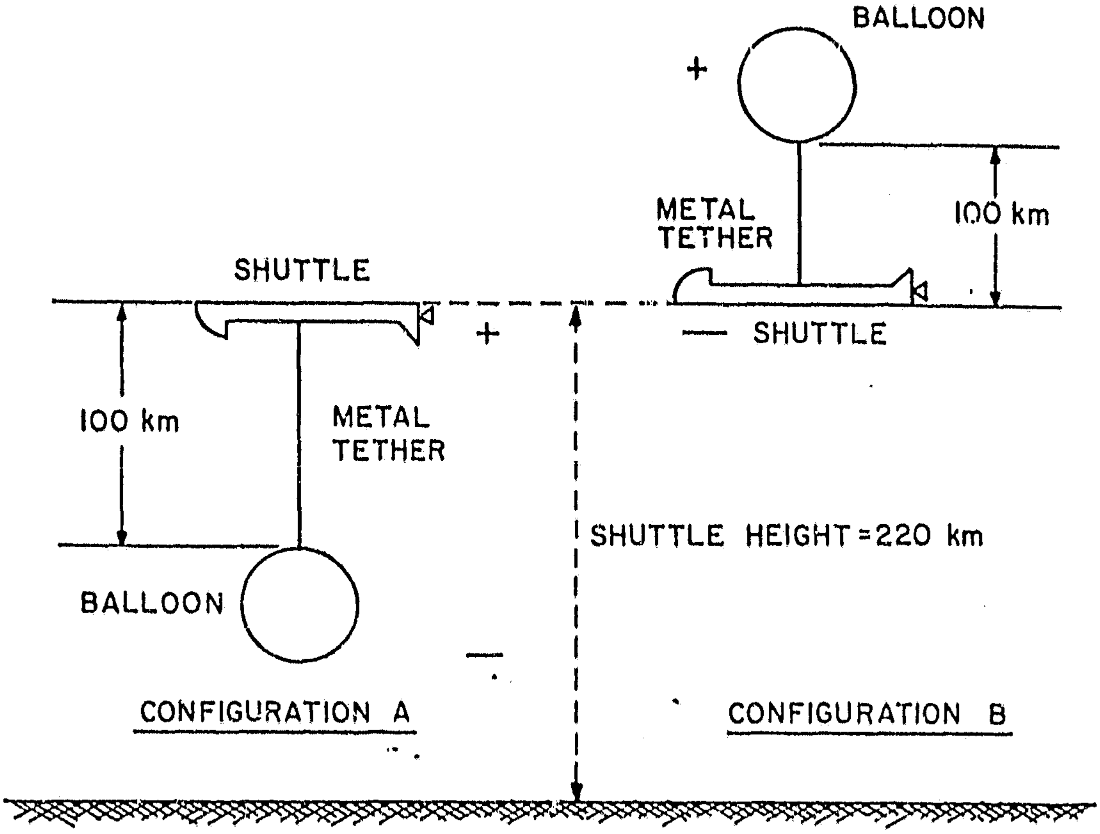

Figure 1. Shuttle-based electrodynamic tether

A long-conducting tether moving in the earth's ionosphere can lead to generation of electromagnetic waves in different frequency bands from ULF to MF, through several mechanisms (Williamson and Banks 1976; Dobrowonly et al., 1979; Dobrowolny 1979; Banks et al., 1980).

(A) Spontaneous Wave Generation

As the tether system moves through the earth's magnetic field, a polarization electric field:

$$\underset{\sim}{E} = -\underset{\sim}{v} \times \underset{\sim}{B}$$

is seen along the tether from the plasma rest frame (we refer, for the moment, to the case of a perfectly conducting tether). With a tether length $L = 100$ km, a Shuttle velocity $v = 7.8$ km/sec, and Earth's magnetic field $B = 0.3$ gauss, we obtain a maximum potential difference between the ends of the system:

$$V_0 = 2.34 \times 10^4 \text{ volts}$$

(for $\underset{\sim}{v} \perp \underset{\sim}{B}$). A corresponding potential difference is therefore seen to be applied between the lines of forces that pass through the terminations of the system and lead to propagation of waves away from the region of the disturbance.

We can speak of "spontaneous" wave generation in the sense that the system is completely passive (no onboard transmitter and no pulsing of its natural current) and the original source of energy is provided by the tether's motion. As has been pointed out (Grossi and Colombo 1978; Dobrowolny 1979), this electrodynamic interaction (and corresponding wave generation) is similar to the interaction of certain celestial bodies with plasmas, like the moon Io of Jupiter, in its motion in the Jovian magnetosphere. Recent Voyager I measurements in the Io's flux tube (Ness et al., 1979) have actually confirmed the occurrence of this interaction.

(B) Driven Wave Generation

Through proper modulation of an electron emitter at the Orbiter, one can obtain pulsating currents in the conducting tether (Banks *et al.*, 1980), which then becomes a long driven antenna. One can also use a transmitter to obtain the pulsating tether current. A transmitter would be necessary in the case of a horizontal tether oriented in the direction of mot [illegible] there is no natural current in the system.

There would be no dynamical problems with this configuration. In fact, the horizontal tether, if terminated at the free end by a balloon (that operates as an aerodynamic brake) would be a stable system configuration (Colombo, 1980).

(C) Generation of Accelerated Electron Beams

In configuration A of Figure 1 (balloon downward with respect to the Shuttle), and under the assumption that the Shuttle is kept at low potentials with respect to the medium, large potential drops may be present between the balloon surface and the ionospheric plasma. Then, as first pointed out by Dobrowolny (1979), secondary electrons can be produced by the impact of energetic ions on the surface of the balloon. These secondaries may then be accelerated away from the balloon along magnetic lines towards Earth's atmosphere. [Emission of photoelectrons from the balloon surface is not of primary significance at the altitudes under consideration (Dobrowolny 1979)]. Thus, generation of accelerated electron beams is another phenomenon that might be associated with the tether's interaction with the surrounding medium. This has been suggested by a number of authors (Goldreich and Lynden-Bell 1969; Gurnett 1972; Hubbard *et al.*, 1976) in studies of the interaction of Io with Jupiter's magnetosphere.

(D) Generation of HF (High Frequency) Electromagnetic Waves

The generation of accelerated electron beams may give rise to instabilities, through electron cyclotron resonance interactions, and may produce whistlers (or even higher frequency waves). At the altitudes of interest, the electron cyclotron frequency is $f_{ce} \sim 0.8$ MHz and the electron plasma frequency

f_{pe} ranges from 5 to 11 MHz. It is therefore in the HF (high frequency) band where we may expect wave generation by accelerated electron beams.

1.3 Plan of the Investigation

As the previous summary indicates, there is a rich phenomenology associated with the electrodynamic tether and, correspondingly, many different associated problems fall under the general heading of wave generation.

Prior to any detailed investigation of the generation of some specific waves, it is essential to be able to calculate, for a given tether configuration, how the primary electrodynamic power available (associated with the $\underline{v} \times \underline{B}$ force) is directed into different channels. In particular, we need to determine how much power is dissipated into ohmic losses in the tether, how much (if any) goes into acceleration of electron beams, and how much is presumably left for wave generation.

We need a model to compute the current-voltage characteristics of the long tether (with end electrodes), taking into account finite resistance of the tether and, where present, the effect of photoelectric or secondary emission. This will be developed in Section 2 of this report. Results will be derived for a passive tether (without ion or electron guns on the Shuttle), for different tether resistances, and as a function of the radius of the conducting balloon that terminates the tether at one end. Some comments and results on the use of electron and ion guns will also be given.

In Section 3 we will consider possible effects connected with secondary accelerated electrons. A discussion of the distribution of emitted secondaries will indicate that the excitation of electromagnetic instabilities is probably not important from the energetic point of view. Excitation of UV radiation by the high-energy electrons at the foot of the tube cut through by the balloon can be an interesting possibility, which is inferred from an analogy with a similar phenomenon measured at the foot of the flux tube of Jupiter's satellite Io.

In Section 4 we will discuss the mechanisms of spontaneous wave generation and the range of frequencies of the electromagnetic disturbance associated with TSS. We will then focus our attention on the generation of low-frequency Alfvèn waves, which requires large balloon dimensions. The physical picture of the Alfvèn wave system associated with the TSS motion will be described. Current along magnetic flux tubes, power, and impedance associated with transmission of Alfvèn waves from the tether will be computed. The Alfvènic current, obtained as a function of balloon radius, will then be compared with the current obtained from the model for particles collected from the plasma by the end electrodes.

In Section 6, on the basis of the calculation of power in Alfvèn waves, we will use theory of wave propagation to the ground for a point dipole source in the ionosphere (despite its inadequacy for our system) to determine the potential for detecting VLF waves at ground level, and will draw a preliminary positive conclusion. Finally, Section 5 will summarize the main points of the report.

2. Studies of Current-Voltage Characteristics of the Electrodynamic Tether

2.1 Model for Charged Particle Collection

The tether-balloon system, moving across magnetic lines, carries a current due to the collection of ionospheric ions and electrons at its ends (the balloon and the conducting part of the Shuttle, which is assumed to have an area of 35 m^2).

The condition that one imposes to derive current and potentials is that of a balance of charged particle fluxes between the two end electrodes. In terms of currents, the current collected at the Shuttle i_s has to be equal and opposite to the current i_B collected at the balloon:

$$i_s(V_s) = -i_B(V_B) \tag{2.1}$$

(for a tether system without any gun, ion or electron, at the Shuttle). In (2.1) we have explicitly indicated that the currents are functions of the potentials (V_S, V_B) of the two electrodes, with respect to the plasma. For a perfectly conducting tether, it would be:

$$|V_S - V_B| = |\underline{v}_o \times \underline{B} \cdot L| \tag{2.2}$$

where $\underline{v}_o$ is the Shuttle velocity (v_o = 7.8 km/sec), $\underline{B}$ is Earth's magnetic field ($B \sim 0.3$ gauss, at the altitudes of interest between 100 and 300 km), and L is the tether's length. Hence (2.1) is an implicit equation for one of the potentials, for example V_S. Having determined V_S,V_B is obtained from (2.2), and then the current $I_c = |i_S| = |i_B|$ is calculated from the solutions found for the potentials.

The model that has been used for charged particle collection is the following (Anderson et al., 1979). For the attracted particle contribution to the current referring to particles of species j (j = i, e for ions and electrons respectively), we write:

$$\frac{i_j \text{ attracted}}{i_{jo}} = f\ (V) \tag{2.3}$$

where the normalizing electron and ion currents are given by:

$$i_{eo} = \frac{1}{8} n_\ell |e|\ v_{the} A \tag{2.4}$$

$$i_{io} = \frac{1}{4} n_\ell Z |e|\ v_o A \tag{2.5}$$

(with A the collecting area, n_ℓ the electron density, and v_{the} thermal velocity). The function f, which depends from the electrode potential V, through:

$$\phi^* = \left|\frac{eV}{kT_e}\right| \left(\frac{\lambda_{de}}{R}\right)^{4/3} \tag{2.6}$$

(T_e being electron temperature, λ_{de} the Debye length, and R the electrode's radius), is plotted in Figure 2. The function f was derived by combining dif-

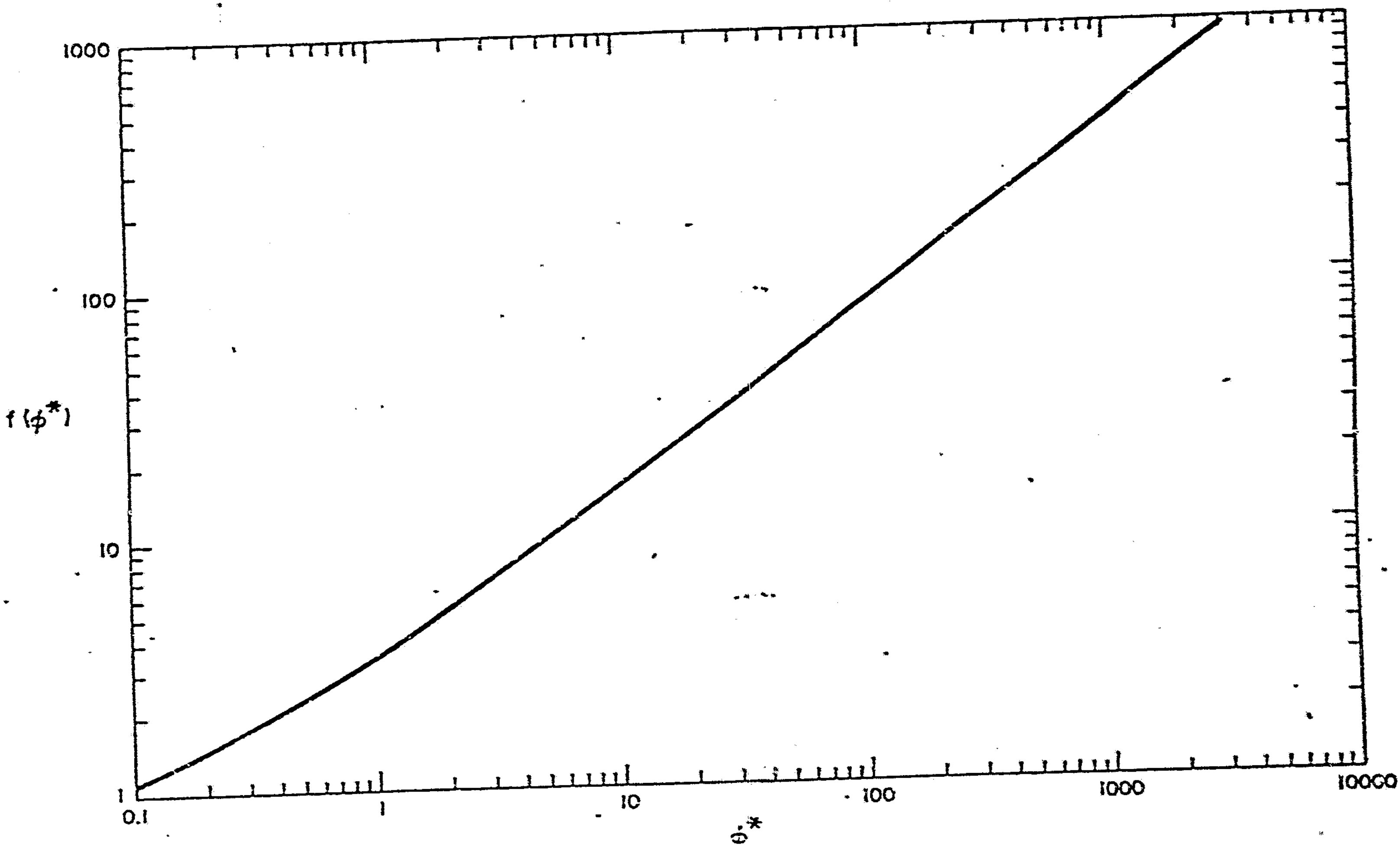

Figure 2. Graph of the Function f(φ*).

ferent models for particle attraction by large electrodes at large and moderate potentials (Alpert et al., 1965; Linson 1969).

For the repelled particle contribution to the current, we used simply:

$$\frac{i_j \text{ repelled}}{i_{jo}} = e^{-\left|\frac{eV}{kT_e}\right|} \tag{2.7}$$

where V is now the repelling potential.

Approximate results for currents and potentials as a function of balloon radius, obtained with the above model for a perfectly conducting tether, are given by Anderson et al. (1979).

Recently, we have developed (1980) a more accurate method, based on a transmission line analogy of the tether system, to compute the stationary state described by (2.1). We did this by solving a time dependent problem, and hence obtained also the transient of the tether system towards the stationary state.

This method, which was devised especially for the more difficult case of computing current and potential distributions of a bare metallic tether, has now been applied to the tether-balloon system under consideration (conducting insulated tether with terminal electrodes), including also the effect of tether resistance and, as will be described, the possible emission of secondary electrons from the lower electrode of the system, and the effects of using electron or ion emitters.

Finally, it should be noticed that the equilibrium current i obtained in the tether through the above mentioned methods is obviously a very non linear function of the equilibrium potential difference (V_S-V_B), also obtained from the calculations. The various results for current and potentials versus balloon radius which will be seen in what follows, do not correspond therefore to a ohmic relation between i and V_S-V_B involving the tether resistance R_W. It is however tre that, in all cases, the currents obtained must be smaller than the ohmic limit that corresponds to the total electromotive potential available, i.e.:

$$i < i_R = \frac{|\underline{v}_o \times B \cdot \underline{L}|}{R_W}$$

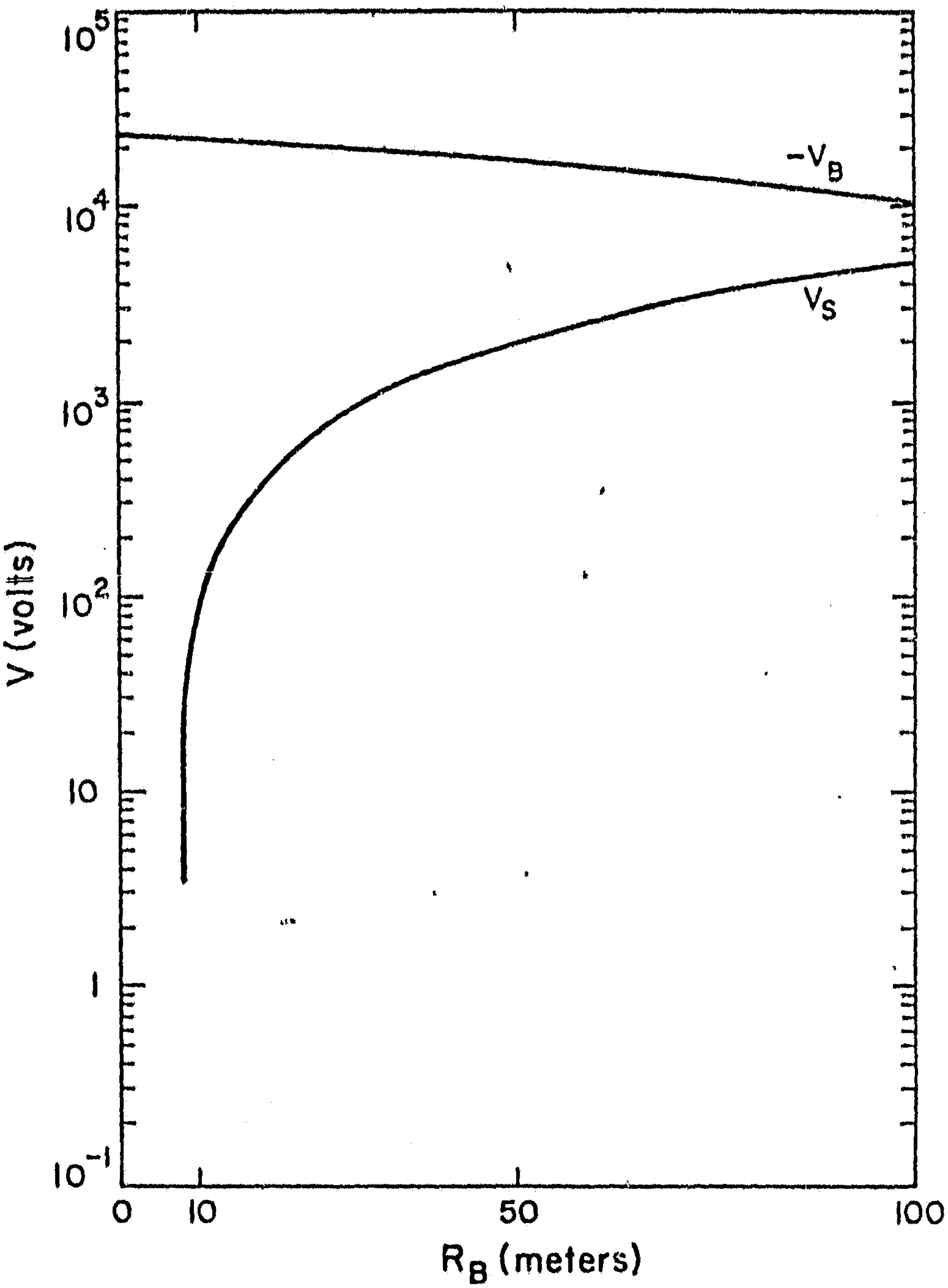

Figure 3. Configuration A : Voltages versus R_B for $L= 10^5$ m, $\rho = 0.03\ \mu\Omega$m

2.2 Results for Current and Voltages

We first present results for current in the tether and voltages of the Shuttle and the balloon for a completely passive system-- i.e., a system not using ion or electron emitters. Figure 3 gives the variations of the Shuttle (V_S) and balloon (V_B) potentials as a function of balloon radius R_B for configuration A (tether deployed downwards) and a resistivity of the tether ρ = 0.03μΩm (aluminum-type tethers). In Figure 4 we have the same quantities for a case of higher resistivity, ρ = 0.15μΩm (piano-steel-wire tether). As can be seen essentially in both cases, the Shuttle potential V_S, which increases with balloon radius, reaches ∿10^2 volts at R_B ∿ 10m. At higher balloon radii, Figure 4, which refers to higher resistance, gives somewhat smaller values for V_S than for the low resistance case of Figure 3.

Another qualitative difference between the results of Figure 3 and Figure 4 is given by the drastic drop in balloon potential $|V_B|$ which occurs at R_B = 85 - 90 m for ρ = 0.15μΩm (see Figure 4), whereas for the lower resistivity ρ = 0.03μΩm, $|V_B|$ decreases with increasing radius but remains relatively high up to the maximum radius (R_B = 100 m) that we have calculated. Clearly, the Shuttle potential must increase with radius in order to balance the increasing current collected by the balloon; eventually, the balloon potential must drop to very low (negative) values. The reason why it does so at smaller radii for the case of the higher resistance depends only upon the increased ohmic losses (at any given radius) that correspond to such higher resistances.

At large balloon radii, as could be necessary to generate larger currents and reach substantial power levels in Alfvèn waves guided by the balloon flux tube (see Section 4), the potential of the Shuttle in such a passive system can be relatively high. The use of an ion emitter at the Orbiter would, therefore, be necessary to keep its potential at low levels.

Figure 5 gives the variation of current in the tether as a function of balloon radius, again for configuration A and the two values of resistivity considered before.

The difference between the two curves of Figure 5 and, in particular, the dip of curve b) (ρ = 0.15μΩm) at R_B = 85 m can be explained in terms of the different behavior of the potential $|V_B|$ as a function of the radius for the two cases considered (see Figures 3 and 4). In the case of the higher resistance, at a radius between 80 and 90 m, the current reaches a quasi-plateau. We understand that on the basis of the formulas for collection efficiency given in Section 2.1, the balloon current is proportional to R_B^2 f $(|V_B|)$. In the region (see Figure 4) where $|V_B|$ drops to small values, the collection efficiency f drops correspondingly. This roughly balances the increase of current with R_B^2 and produces the plateau. Once $|V_B|$ has dropped to small values $(|\frac{e}{k}\frac{V_B}{T_e}| \lesssim 1)$, f $(|V_B|)$ is essentially 1 (see Figure 2) and the current starts increasing again (as R_B^2). This explains the dip of curve b) in Figure 5. The same effect is not present in curve a) because, for the case of the smaller resistivity (ρ = 0.03μΩm) there is no drop in $|V_B|$ for $R_B \lesssim$ 100 m, as seen in Figure 3.

The same quantities (i.e., voltages and current) are plotted in Figures 6 and 7 respectively, referring now to configuration B (tether deployed upward) and for a resistivity ρ = 0.15μΩm. The curves for the smaller resistance are not very different. These results are interesting because they show that, even with small radii of the balloon (or subsatellite)-- e.g., $R_B \sim$ 1m-- in a passive system, the Shuttle goes to high potentials with respect to the plamsa $(|V_S| \sim 10^3$ volts), while the corresponding current is quite small ($i \sim 0.08$ amps). The physical reason for this is the fact that the balloon collects now electrons. In order to balance this electron current, the Shuttle, which collects the much less mobile ions with its collecting area of 35 m^2, must necessarily charge to a high potential. Clearly, the use of an electron gun at the Shuttle is strictly necessary for configuration B-- both to keep the Shuttle potential low and to obtain larger currents.

With either configuration (and also with or without the effect of secondary electron emission), the primary limitation on tether current is seen to be the resistance of the tether. For the two values of resistivity

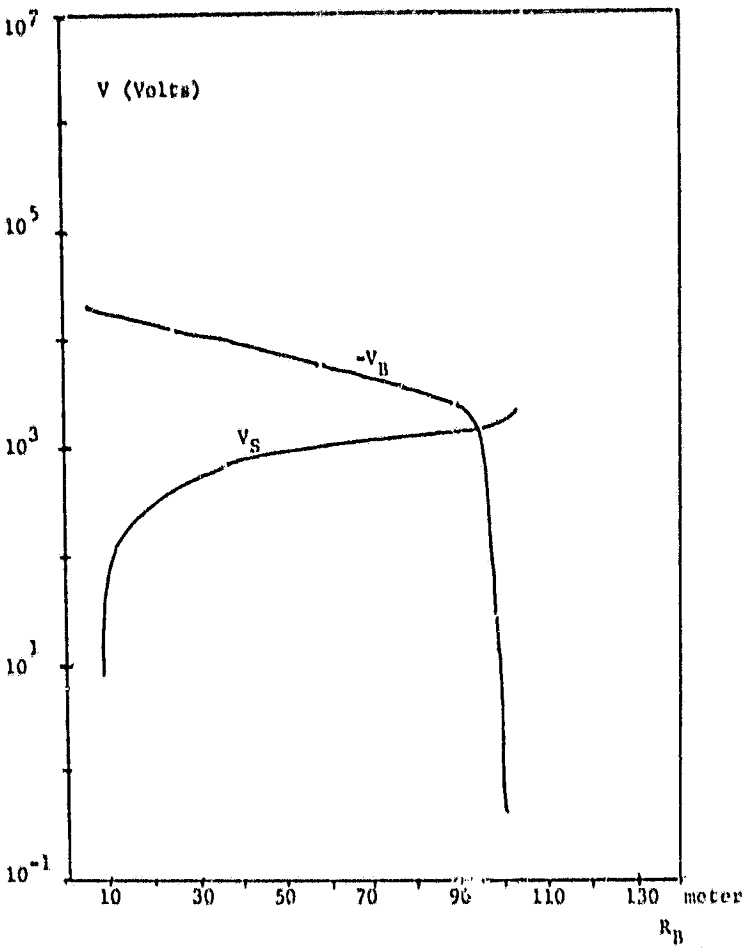

Figure 4 , Voltages versus R_B, Configuration A, L = 10^5m, ρ = 0.15 $\mu\Omega$m.

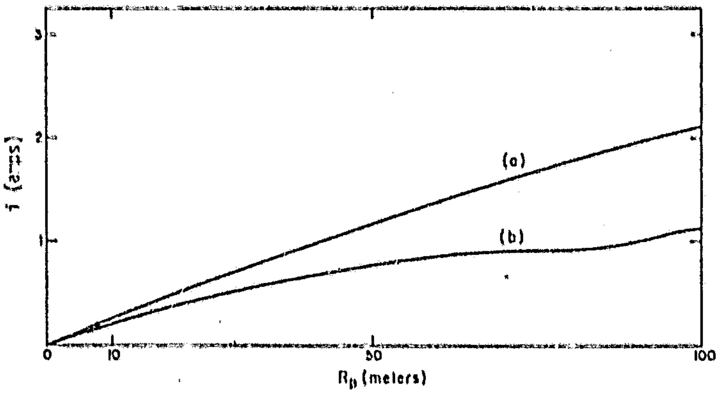

Figure 5, Configuration A : current versus R_B for L = 10^5 m.
(a) ρ = 0.03 $\mu\Omega$m ; (b) ρ = 0.15 $\mu\Omega$m

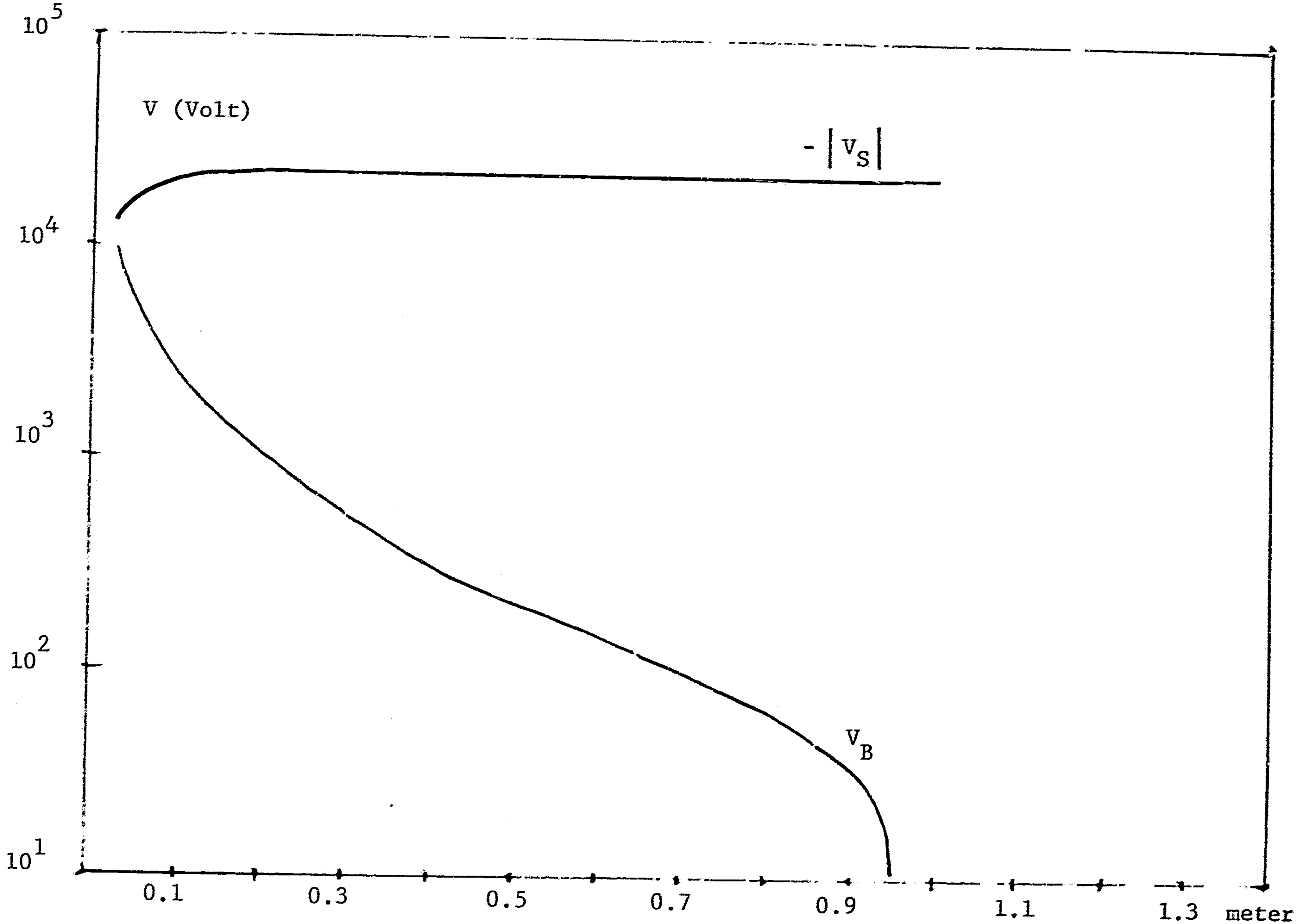

Figure 6. Voltages versus R_B , Configuration B, L = 100 Km, $\rho = 0.15\ \mu\Omega m$.

considered, the limiting values are:

$$i_R = 1.23 \text{ amps} \quad \text{for } \rho = 0.15\mu\Omega m$$

$$i_R = 6.1 \text{ amps} \quad \text{for } \rho = 0.03\mu\Omega m$$

From the curves of Figures 5 and 7, we see that these limiting values are not reached for a passive system, even at large balloon radii. Such values will, therefore, be approached only through the use of charged particle guns.

2.3 Electrical Currents with the use of Charged Particle Guns at the Orbiter

Referring to configuration A, suppose we want to use an ion gun at the Shuttle in such a way as to keep its potential with respect to the plasma at very small values ($V_S \sim 0$). Then the balloon will be, approximately, at a potential $-|V_B|$ where:

$$|V_B| = \Delta\phi_o - R_w i \qquad (2.8)$$

and $\Delta\phi_o = |\underline{v}_o \times \underline{B} \cdot L|$. The current i will be given by (see Section 2.1):

$$i = i_B = i_{io} f(|V_B|) \qquad (2.9)$$

For a given balloon radius R_B, the actual values of current in the tether and potential of the balloon are obtained from the intersection of the two curves $i(V_B)$ given by (2.8) and (2.9).

The result for the current as a function of balloon radius is given in Figure 8. The interpretation is that, for a given balloon radius R_B, an ion gun at the Shuttle with current $i(R_B)$ obtained from Figure 8 is necessary in order to keep the Shuttle at essentially zero potential. The curve, which refers to the low resistivity tether ($\rho = 0.03\mu\Omega m$), gives obviously larger currents than those obtained for configuration A and a purely passive system (see Figure 5).

In the same way we have obtained in Figure 9 the current of an electron gun necessary, in configuration B, to keep the Shuttle potential at low levels.

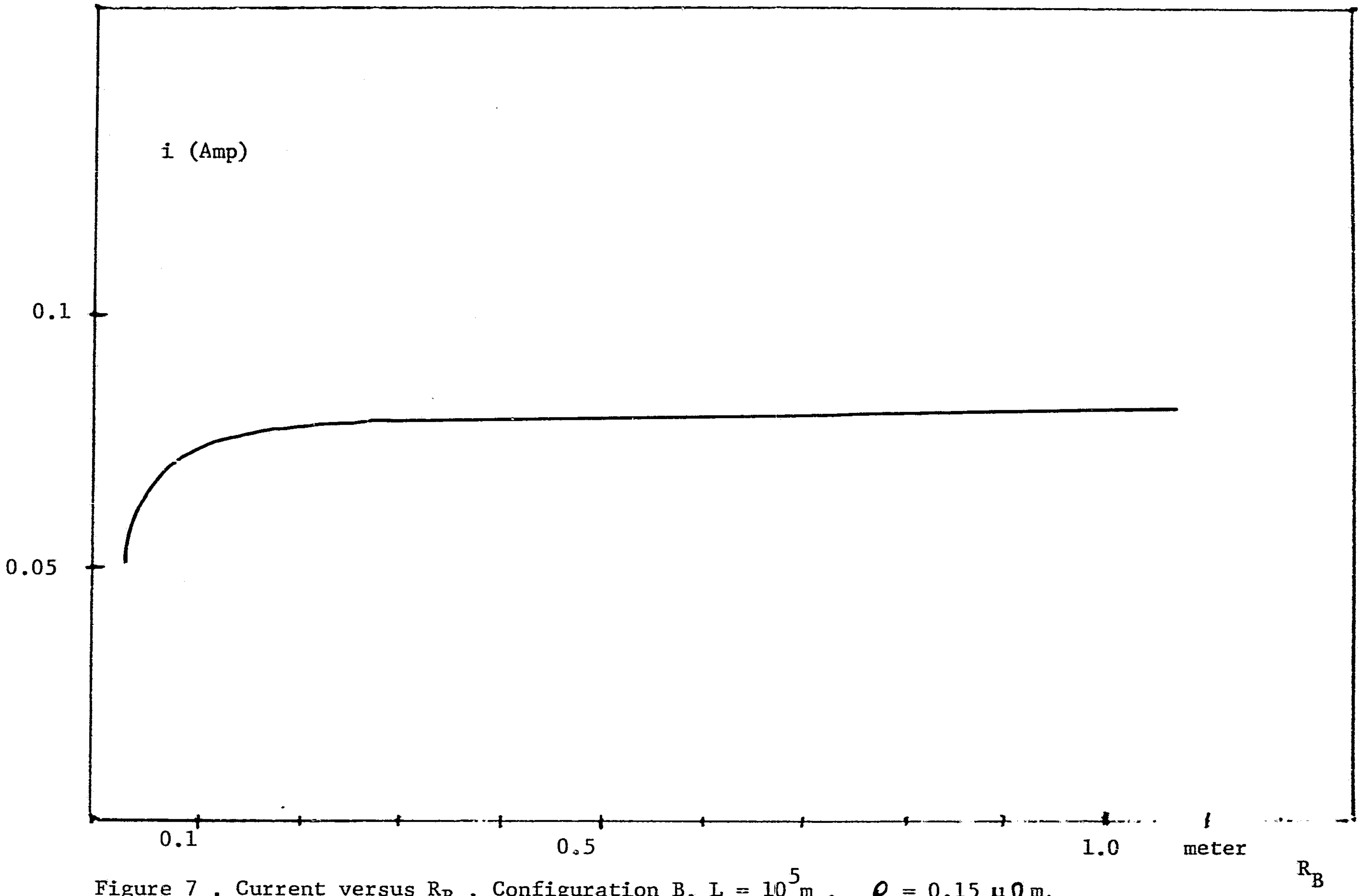

Figure 7 . Current versus R_B , Configuration B, $L = 10^5$ m , $\rho = 0.15\ \mu\Omega$ m.

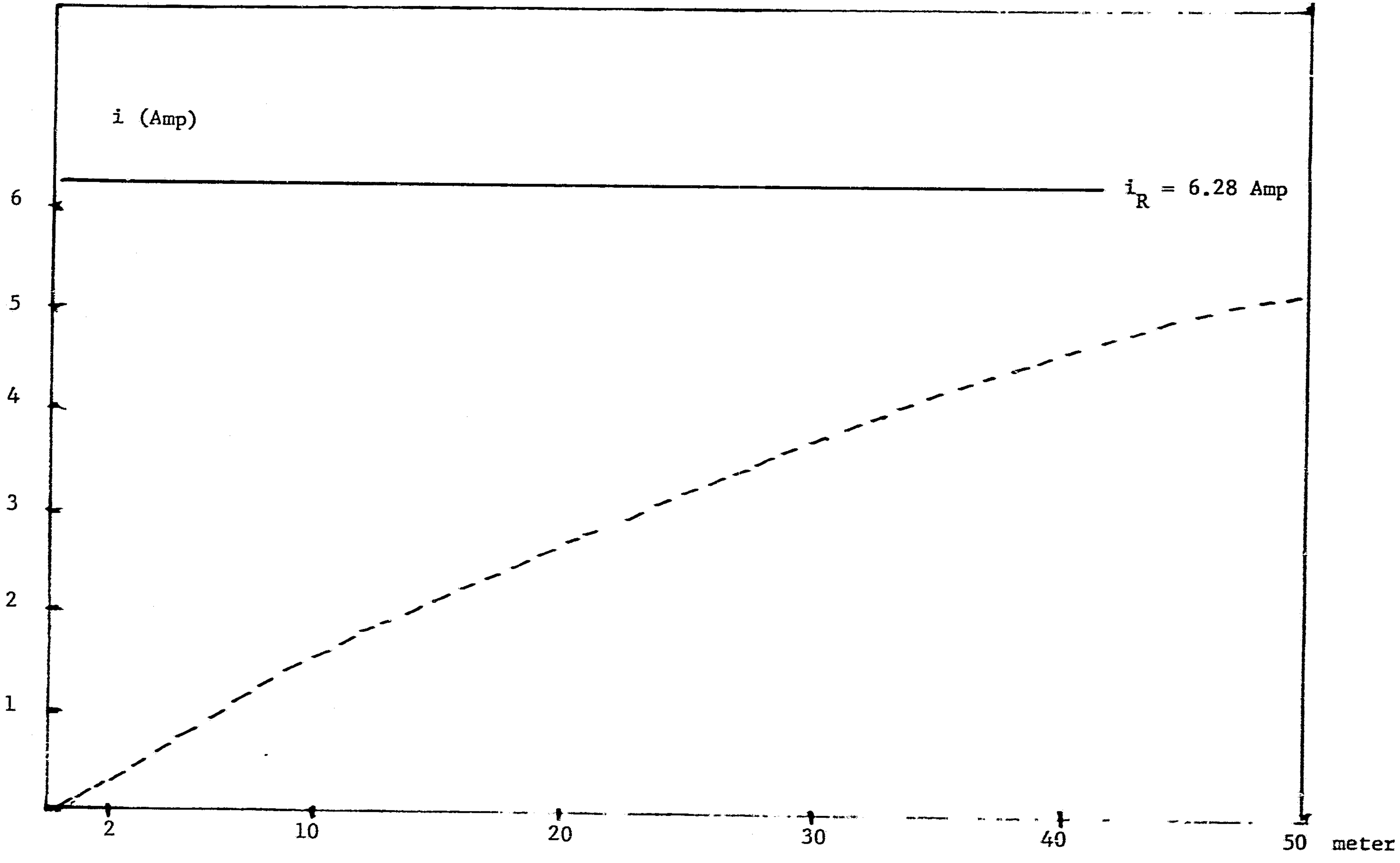

Figure 8 . Currents versus R_B ,Configuration A, L = 100 Km, $\rho = 0.03\ \mu\Omega m$, $r_W = 0.5$ mm. There is an ion gun onboard the Shuttle, so that $V_S \cong 0$.

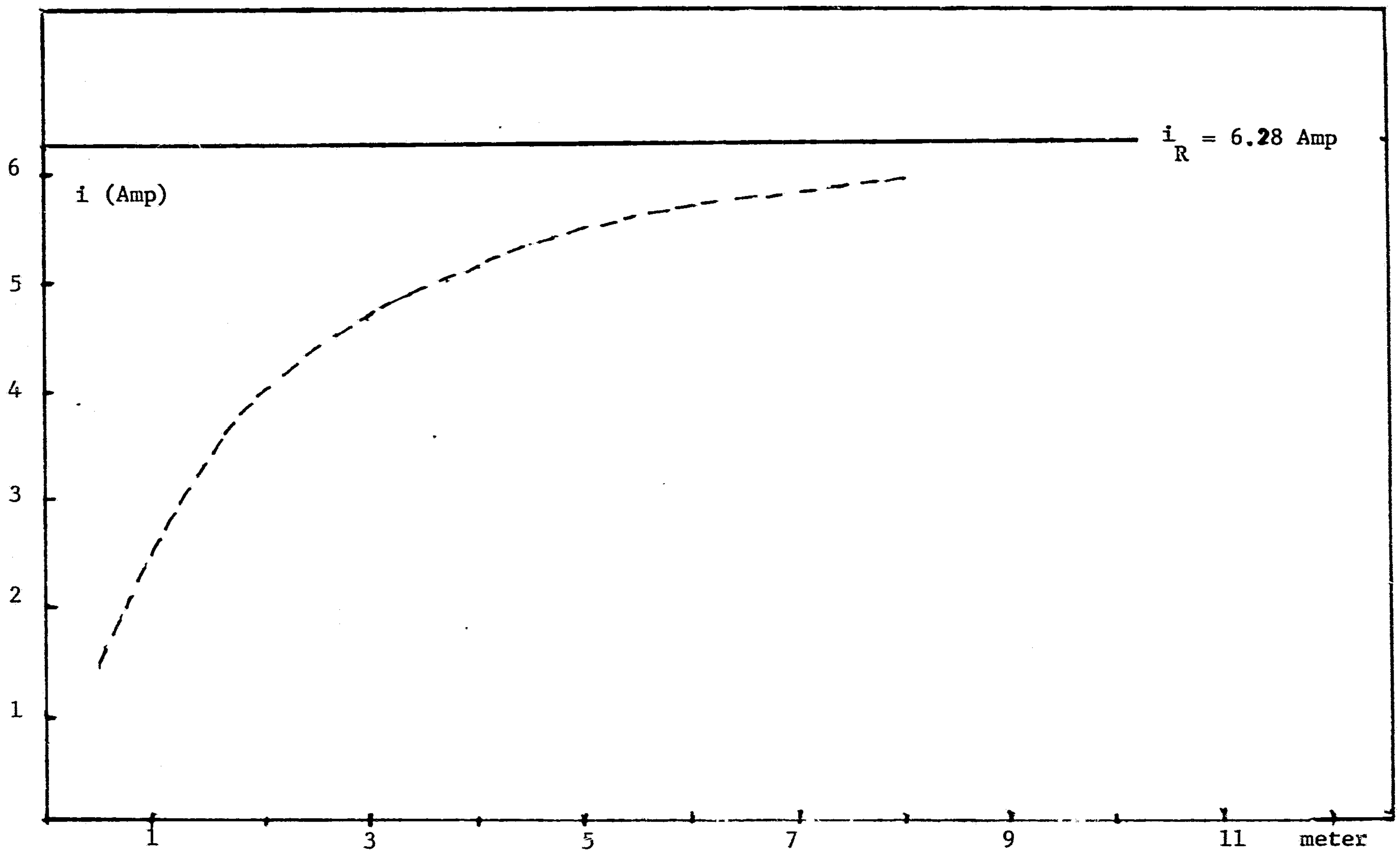

Figure 9. Currents versus R_B , Configuration B, L= 100 Km, $\rho = 0.03\ \mu\Omega$m, r_w =0.5 mm. An electron gun is onboard the Shuttle, so that $V_S \cong 0$.

Comparing with Figure 7, referring to a passive system, we see that the use of an electron gun for configuration B, besides being necessary to keep the Shuttle potential low, is the only way to obtain significant current values regarding electromagnetic wave generation (for example, using the long tether as a dipole antenna). For balloon radii $R_B > 10m$, one already approaches the resistive limitation ($i_R \sim 6.1$ amps).

2.4 Emission of Secondary Electrons by Proton Impact on the Balloon Surface

As can be seen from Figures 3 and 4, referring to a passive system, the downward balloon (configuration A) can be charged to a very high and negative potential. This is, of course, true also if we use an ion gun at the Shuttle to keep its potential low, unless the current of the gun approaches the resistive limit.

In these conditions, the ions impacting on the balloon surface can reach high energies through the accelerating sheath region surrounding the balloon, and then can cause significant emission of secondary electrons. Since this effect will vary the current, and hence the voltages, in the system, it has to be taken into account in computing current-voltage characteristics. The effect is also of interest because the secondary electrons, accelerated away from the balloon through the sheath region, could produce electromagnetic waves (as mentioned in the Introduction).

We will come back to this second aspect later. For now we will focus on how to take the effect of secondary emission into account in our calculation of current-voltage characteristics.

For a given material of the balloon surface, the yield of secondary electrons per ion impact will depend on the energy of the impacting ion and on its angle of impact, with respect to the normal to the surface (Massey and Burhop 1952, McDaniel 1964). In order to discuss how this energy depends upon the potential V_B of the balloon with respect to the plasma, we have to consider the ion motion in the sheath region. First of all, we can suppose the sheath electric field to be radial; this is justified by the fact that wave effects are probably not important as:

$$\frac{1}{2} m_i v_o^2 \ll |eV_B|$$

$(\frac{1}{2} m_i v_o^2 \sim 5\text{eV},\ |eV_B| \sim 2.3 \times 10^4\ \text{eV})$.

For high balloon potentials, we can write for the sheath thickness R_{sheath} (Alpert 1965, Dobrowolny 1979):

$$\frac{R_{sheath}}{R_B} \sim 0.8 \left\{ \left|\frac{eV_B}{KT}\right| \left(\frac{\lambda_{de}}{R_B}\right)^{4/3} \right\}^{3/7} \tag{2.10}$$

Using parameter values for an altitude of approximately h = 120 km (the altitude of the balloon) and using the results for the potential $|V_B|$ shown in Figure 3 (for $\rho = 0.03 \mu\Omega m$), we obtain for the thickness of the sheath, as a function of balloon radius, the values reported in Table I. For comparison, the ion Larmor radius (O^+ ions) and the electron Larmor radius are given by:

$$R_i \sim 4.7\ \text{m} \quad , \quad R_e \sim 2.7 \times 10^{-2}\ \text{m}$$

If we now go to the equation of motion:

$$mi \frac{dv}{dt} = q\ [\underline{E}\ (\underline{R}) + \underline{v} \times \underline{B}] \tag{2.11}$$

and compare the electrical and Lorentz force, we have, in order of magnitude:

$$\frac{E}{vB} > \frac{E}{v_{max} B} = \alpha \tag{2.12}$$

where:

$$\frac{1}{2} m_i v_{max}^2 = |eV_B| \tag{2.13}$$

is the maximum energy the ions can pick up through the sheath region. Estimating:

$$E \sim \frac{V_B}{R_{sheath}}$$

we obtain:

$$\alpha = \left(\frac{m_i}{2e}\right)^{1/2} \frac{V_B{}^{1/2}}{BR_{sheath}} \sim 9.6 \frac{V_B{}^{1/2}}{R_{sheath}} \qquad (2.14)$$

The values of α corresponding to various values of balloon radii are also reported in Table I. It is $\alpha > 1$ and, therefore, the electrical force dominates in the equation of motion (2.11). In these conditions, we have a radially accelerated motion and all the ions entering the sheath region will finally pick up the energy (2.13) corresponding to the potential drop $|V_B|$ between the balloon and the plasma (and all of them will normally hit the surface).

Hence, in the stationary state, the current balance condition (2.1) (for configuration A) can now be rewritten, taking secondary emission into account as:

$$i = i^{(e)}\ (V_s) = -i^{(i)}\ (V_b)\ [1 + \delta\ (|V_B|)] \qquad (2.15)$$

where the yield δ is a function of the total balloon potential with respect to the plasma.

Table I

Values of the Parameter α

R_B (meters)	$\|V_B\|$ (volts)	R_{sheath} (meters)	α
1	2.33×10^4	7.1	2.07×10^2
5	2.29×10^4	14.07	1.04×10^2
10	2.24×10^4	18.74	7.69×10^1
20	2.11×10^4	24.59	5.69×10^1
30	1.96×10^4	28.34	4.76×10^1
50	1.69×10^4	33.15	3.78×10^1

2.5 Discussion of a Model for the Yield in Secondary Electrons

The main problem now is the choice of the function $\delta(V_B)$. To our knowledge, there are essentially no data on secondary emission from impacting O^+ ions (the dominant species in the ionosphere at the altitudes of interest). Besides, the data available are, in general, very scarce for any ion (not only O^+) in the range of energies from 1 to 20 keV, where the effect of secondary emission could be significant.

Figure 10 gives the yield as a function of energy for protons impacting on two different materials. The yield was obtained by Whipple (1965) by putting together data from different experiments, at various energies, including the range of interest here. Although we do not have an analogous curve for O^+ ions, we can still derive from the existing literature on secondary phenomena (McDaniel 1964) some useful information on the variation of the yield, with impact on mass at various energies.

What one finds is that, at low energies (<1 keV, approximately), the yield decreases with mass (see curves referring to ions of various noble gases by Hagstrum 1956). On the other hand, for very high energies (>100 keV), the yield seems to be almost proportional to the mass (Massey and Burhop 1952, McDaniel 1964). There are almost no results for intermediate keV energies, where the two dependencies from mass (that appropriate for very low energies and that for very high energies) should obviously merge into one another. Figure 11, taken from Higetsherger et al. (1956), goes up to 8 keV, includes O^+ ions, and indicates a smaller yield for increasing mass.

On the basis of this information, we will use in the following study of current-voltage characteristics the Whipple's curve of Figure 10, referring to protons (and the aluminum target). The discussion indicates that, in the range 1 keV - 20 keV, this curve may give an overestimate. For energies lower than ∿1 keV, where the yield decreases strongly with mass, the use of the proton

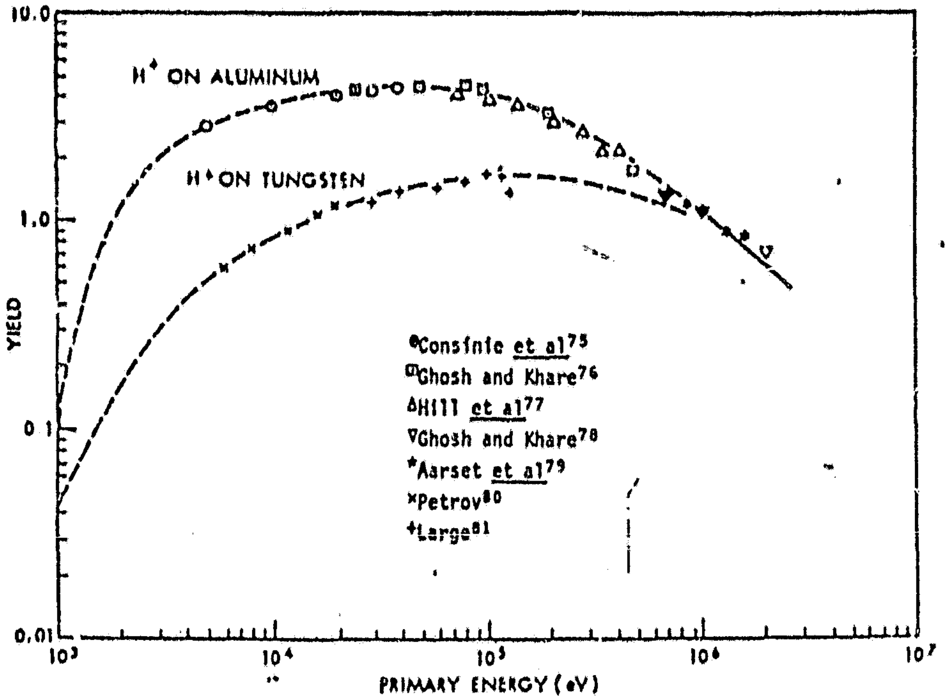

Figure 10. Secondary yield of electrons for proton impact at energies above 1 KeV (from Whipple, 1965).

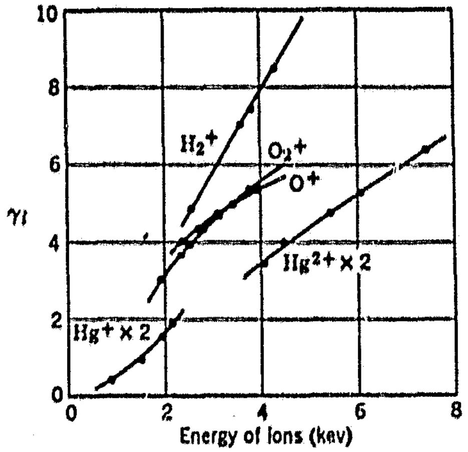

Figure 11. Electron yields of various ions on Ag-Mg targets (from M.J. Higatsberger, H.L. Demorest, and A.O. Nier, J. Appl. Phys. 25, 883, 1954).

curve certainly represents an overestimate. On the other hand, for these potential values, the yield (for protons as well) is already quite small and does not have any appreciable effect on current-voltage characteristics.

2.6 Results for Current and Voltages in Presence of Secondary Electron Emission

Figures 12 and 13 give the Shuttle and balloon voltages as a function of balloon radius, with secondary electron emission taken into account. They refer respectively to the two values $\rho = 0.03 \mu\Omega m$ and $\rho = 0.15 \mu\Omega m$ of the resistivity of the tether. They should be compared with the curves of Figures 3 and 4, referring also to a passive system, and configuration A, but not taking the effect of secondary emission into account.

Figure 14 gives current as a function of balloon radius for the two previous values of resistivity, and includes the effect of secondary electrons.

Emission of secondaries increases the current, as can be seen by comparing the curves of Figure 14 with the corresponding curves of Figure 5. For example, for $\rho = 0.03 \mu\Omega m$ and $R_B = 10$ m, the current goes from 0.23 amps to 0.98 amps when secondary emission is taken into account. The increased current, which leads to greater ohmic losses, tends to lower the balloon potential and hence transfer some of the potential drop to the Shuttle. This effect cannot, however, be very large; in such a case, the emission of secondaries, and hence the current, would start decreasing. Comparing potential values for corresponding balloon radii between Figures 3-4 and 12-13, we can see that there is in fact some displacement of potentials in the sense mentioned above. In spite of the fact that the effect of secondaries is probably overestimated, these variations are nonetheless rather small.

Notice that the curve b) in Figure 14 (that refers to $\rho = 0.15 \mu\Omega m$) shows a monotonic behavior contrary to the corresponding curve in Figure 5. The reason for the difference is that, when the balloon potential drops to very low values (that explain the feature of curve b) in Figure 5), the contribution to current due to secondary electrons drops to zero. The change in slope of curve b) in Figure 5 does not appear in Figure 14 because of the effect above.

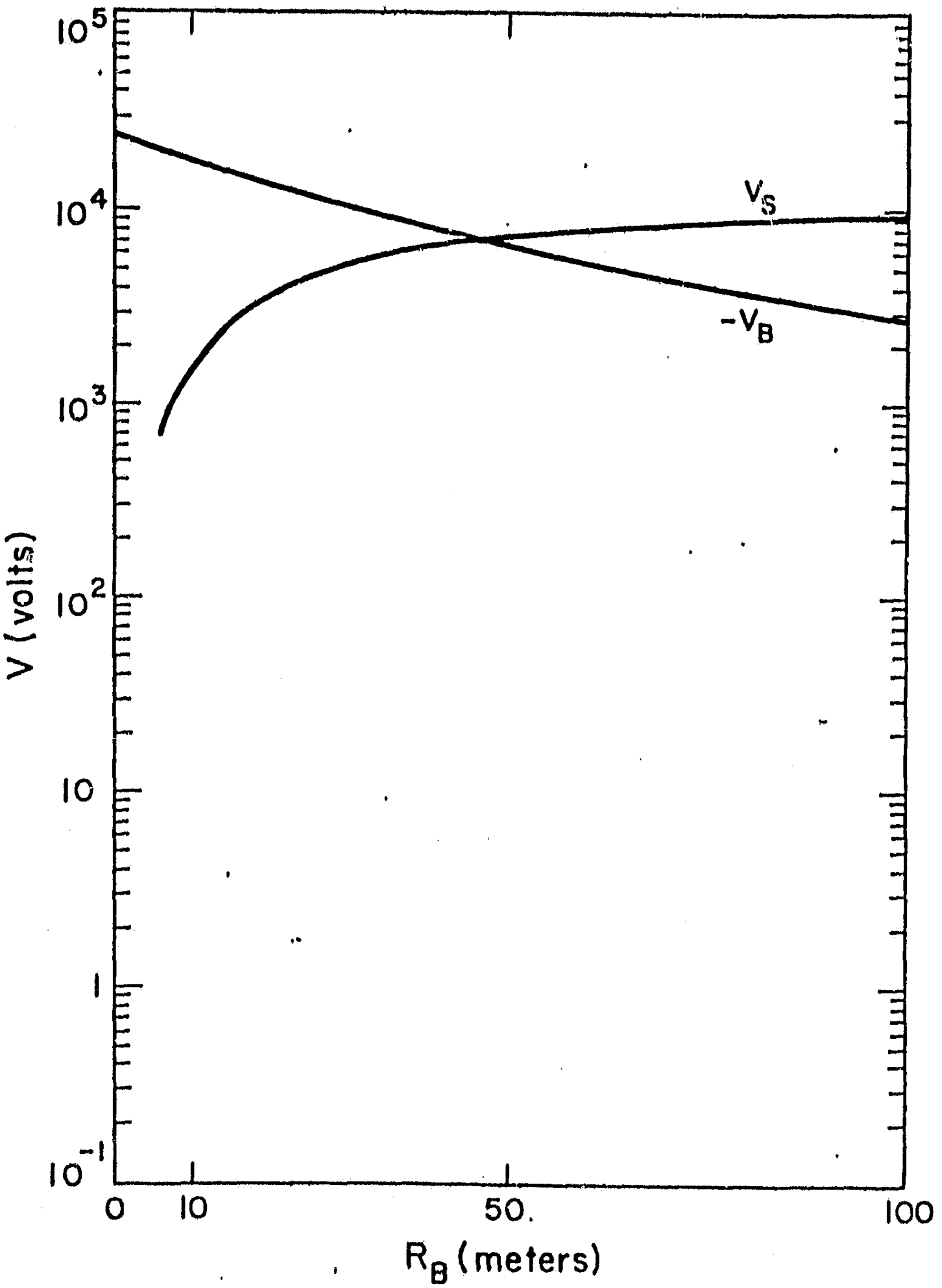

Figure 12. Configuration A : Voltages versus R_B taking secondary electron emission into account for L= 10^5 m, ρ =0.03 $\mu\Omega$m.

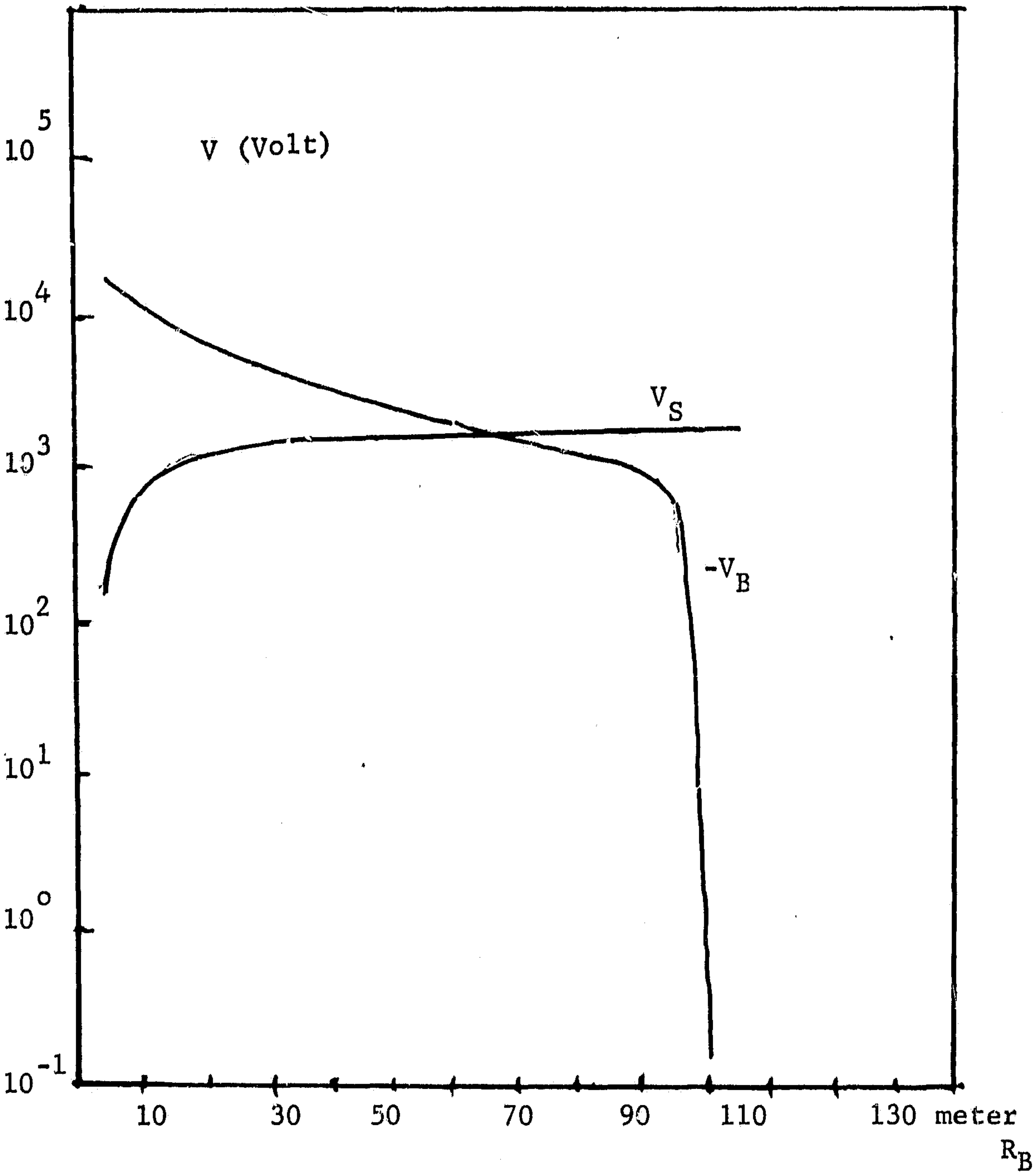

Figure 13. Voltages versus R_B, taking into account secondary electron emission, Configuration A, $L = 10^5$ m, $\rho = 0.15\ \mu\Omega$m.

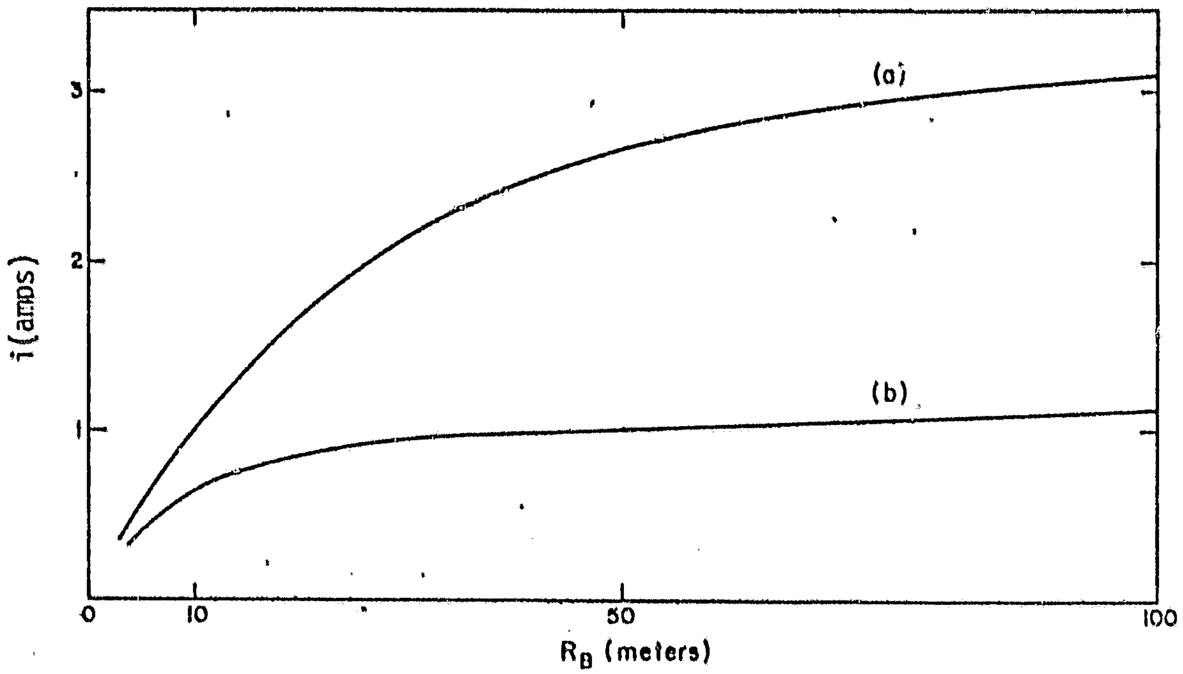

Figure 14. Configuration A : current versus R_B for $L = 10^5$m and taking secondary electron emissions into account.
(a) $\rho = 0.03\ \mu\Omega m$ (b) $\rho = 0.15\ \mu\Omega m$

2.7 Partition of Primary Electrodynamic Power into Different Loads

Prior to detailed investigation of any specific mechanisms or effect of the tether's electrodynamic interactions, it is of fundamental importance to understand how the primary electrodynamic power of the tether system (coming from the $\underline{v}_0 \times \underline{B}$ electric field) is divided into different loads.

The power that we calculate from:

$$P_1 = |V_s - V_b| i \tag{2.16}$$

by using the results obtained for current and potentials, does contain the effect of ohmic losses in the tether (i.e., $|V_s - V_b| = V_o - R_w i$). The ohmically dissipated power is given by:

$$P_2 = R_w i^2 \tag{2.17}$$

If there is no effect of secondary electron emission, we can say that the total power P_4 available for exciting wave processes outside the tether is equal to P_1. That is:

$$P_4 = P_1 \tag{2.18}$$

Where acceleration of secondary electrons takes place, an overestimate for the power P_3 in accelerated electrons is obtained by supposing that, in passing through the sheath surrounding the balloon, the electrons gain all the energy $|eV_B|$. Then:

$$P_3 = |V_B| \, i_{sec} \tag{2.19}$$

with i_{sec} the current in secondary electrons. This is indeed an overestimate, partly because the emitted secondaries are accelerated through the sheath region only through the component of the electric field parallel to $\underline{B}$, which adds a numerical factor (<1) to the above formula. Since our treatment of the secondary emission is an approximate one (see Section 2.5), and since the current is also overestimated, we will use (2.19) as it is. There:

$$i_{sec} = i^{(i)} (V_B) \delta (|V_B|) \tag{2.20}$$

At the equilibrium state we can use (2.15) to obtain, in terms of the total current i:

$$i_{sec} = i \frac{\delta(V_B)}{1 + \delta (V_B)} \tag{2.21}$$

and, correspondingly:

$$P_3 = |V_B| \; i \frac{\delta}{1+\delta} \tag{2.22}$$

In the general case $P_3 \neq 0$, the power P_4, which is available for wave generation, is given by:

$$P_4 = P_1 - P_3 \tag{2.23}$$

More precisely, P_4 is power going into wave generation (once, for example, the tether current is pulsated), if there are no other dissipative phenomena. Generation of microturbulence in the charged sheath surrounding the balloon could absorb power. Thus, P_4 must be considered to be rather an upper limit for the power available to wave generation.

2.8 Results for Different Power Levels

Figures 15 through 18 give the results for the computation of the power levels P_2, P_3, and P_4 as a function of balloon radius for a passive system (configuration A) and both with and without the acceleration of secondary electrons. Again, the two values of resistivity ($\rho = 0.03\mu\Omega m$ and $\rho = 0.15\mu\Omega m$) are considered.

The following important points can be made from these results:

(a) Even with high values of current (obtained for large values of R_B) and in spite of the high ohmic losses, the power P_4 available for wave generation is substantial, of the order of several kilowatts (even for the case of higher resistance; see Figures 17 and 18).

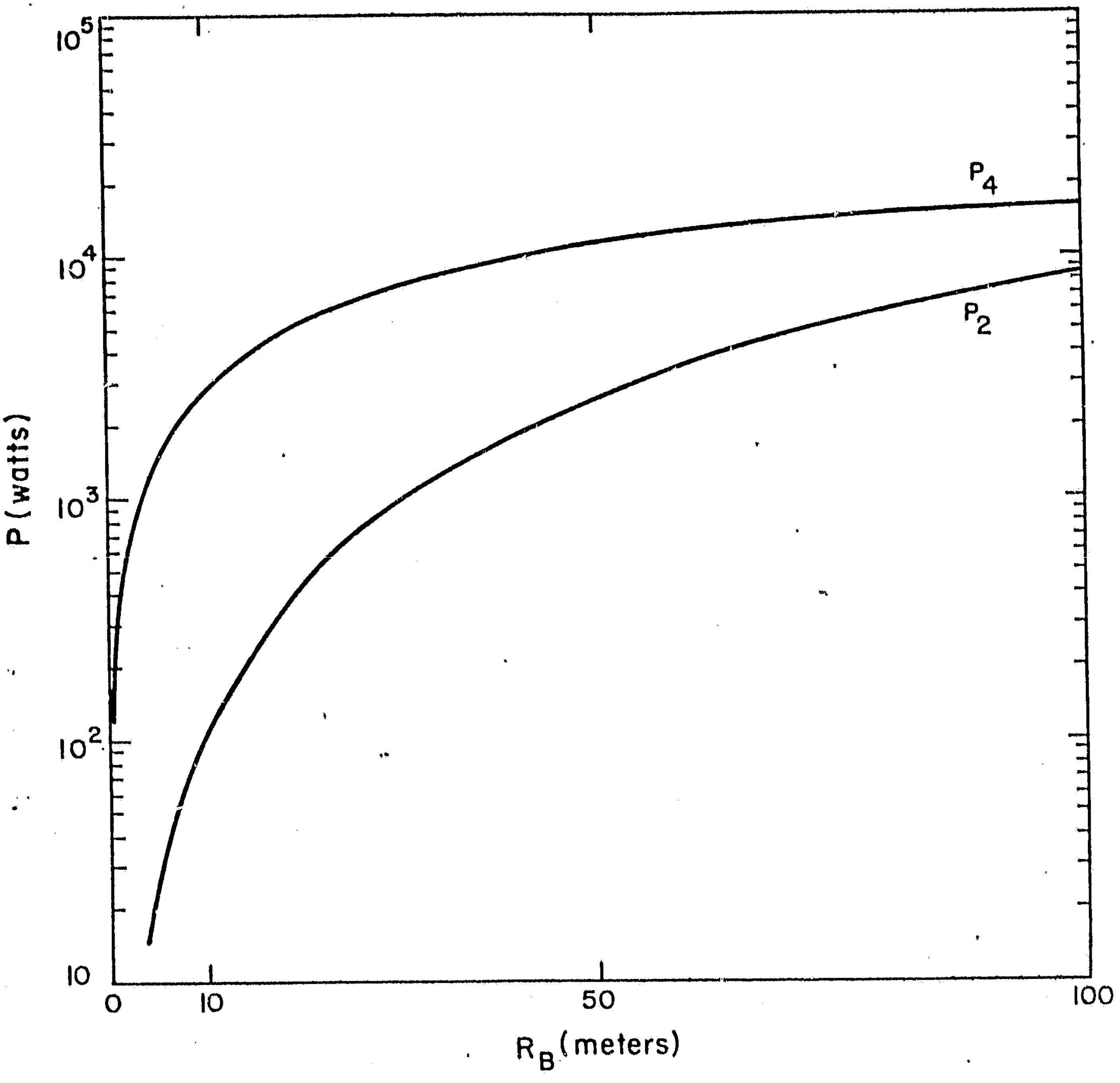

Figure 15. Power into ohmic dissipation (P_2) and into wave radiation (P_4) without effects of secondary electrons. Configuration A, $L = 10^5$m, $\rho = 0.03\ \mu\Omega$m.

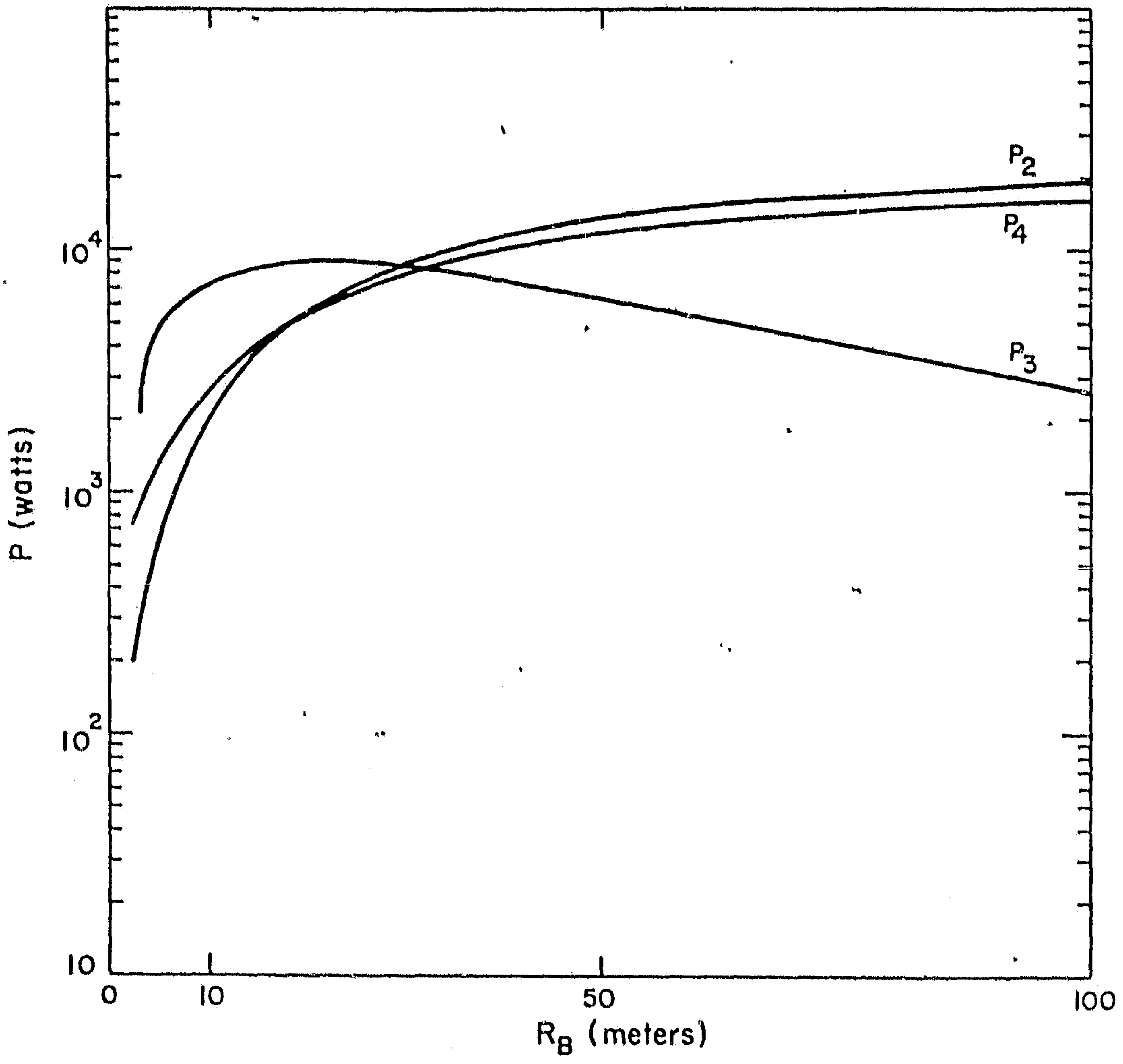

Figure 16. Power into ohmic dissipation (P_2), acceleration of secondary electrons (P_3) and wave radiation (P_4) : configuration A, $L= 10^5$m , ρ =0.03 $\mu\Omega$m.

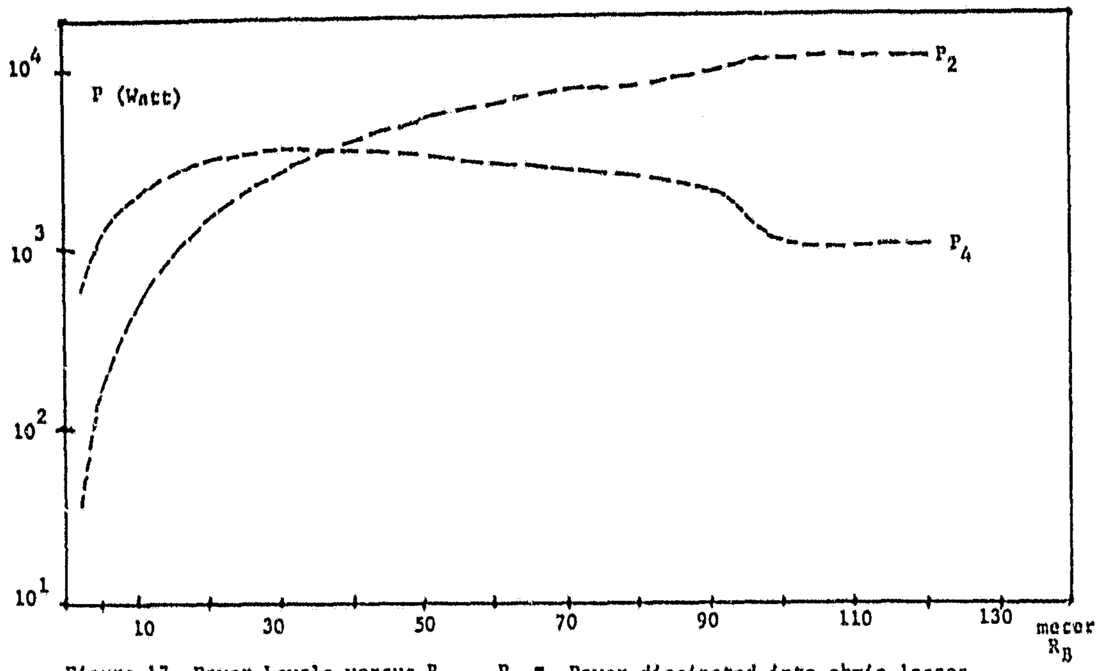

Figure 17. Power Levels versus R_B, P_2 = Power dissipated into ohmic losses, P_4 = Power that goes into e.m. wave radiation ; no effect of secondary electrons is taken into account; Configuration A, L= 10^5 m, ρ = 0.15 $\mu\Omega$m.

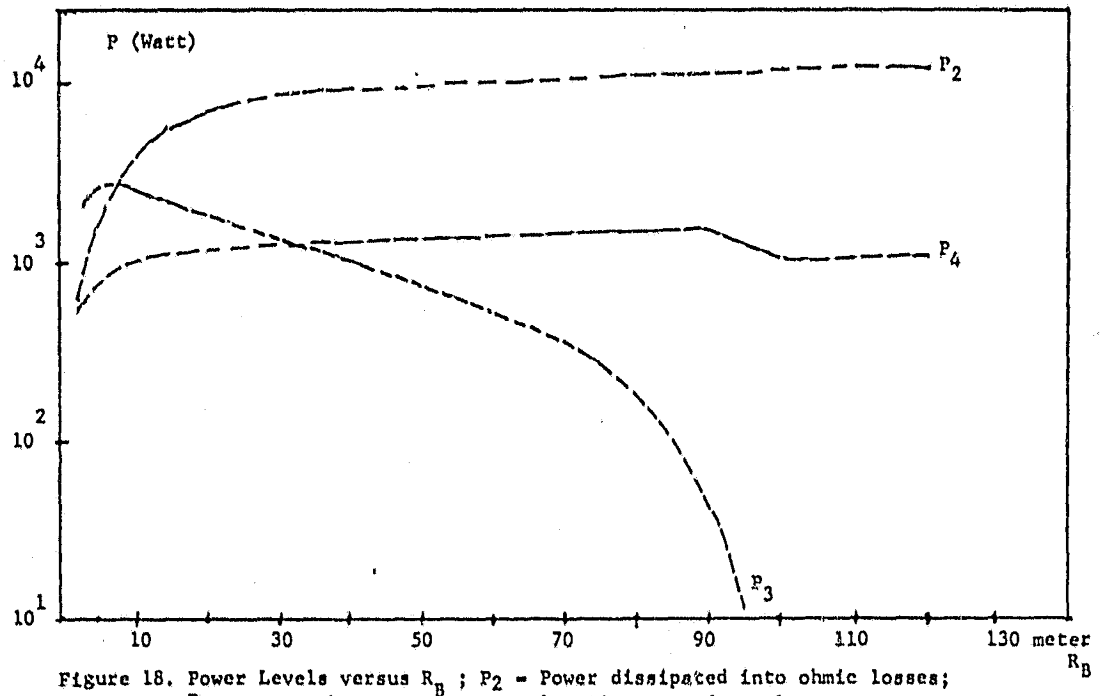

Figure 18. Power Levels versus R_B ; P_2 = Power dissipated into ohmic losses; P_3 = Power that goes into accelerating secondary electrons ; P_4 = Power that goes into e.m. wave radiation; Configuration A, L = 10^5 m; ρ = 0.15 $\mu\Omega$m.

(b) The power P_3, which goes into acceleration of secondary electrons is also significant. It amounts to several kilowatts-- even at very large radii for the low resistance case (see Figure 16)-- whereas it drops to lower values for larger radii, due to the higher ohmic losses, in the case of higher resistance (see Figure 18). Even in this last case, $P_3 > 10^3$ watts up to radii $R_B < 30$ m. Although this power, as it comes from the previous discussion, is certainly overestimated, its values make it potentially interesting to discuss effects produced in the medium by the accelerated secondary electrons.

(c) If we compare the wave power P_4, obtained with and without secondary emission effects, we see that the effects are not much different.

Substantial power levels are therefore available for wave generation, even if the effects of secondary electron production and acceleration are taken into account. This important conclusion would stand even in a more exact treatment of the problem, because it comes from an overestimate of the effect of secondary electrons. It is clearly a very significant conclusion in terms of the capability of the long tether to radiate electromagnetic waves.

Besides these general conclusions, it is worth to comment on the behavior of the curves P_4 that represent the power available for wave radiation, in Figure 17 and Figure 18 ($\rho = 0.15 \mu\Omega m$). In these Figures, we have performed calculations using larger balloon radii than in the previous Figures. In both cases there is a decrease in P_4 starting with a radius of about 90 m, while P_4, and the ohmic power loss P_2 as well, go to an asymptotic value for radii $R_B \geq 100$ m. This can be understood in terms of the current balance that we are imposing, and of the formulas for current collection that were given in Section 2.1. A consequence of these is that both $|V_S - V_B|$ and the current i go necessarily to asymptotic values for large enough values of R_B. What happens is that, for ρ = 0.15μΩm and $R_B \cong$ 90 m, the balloon potential $|V_B|$ drops to very low and negative values (see Figure 4). If $|V_B|$ continues to drop from these low values, some electrons start to be collected at the balloon (in spite of its repulsion potential). This causes a decrease in current and explains the decrease in P_4 around the value $R_B \cong$ 95 m, as seen in Figure 17 and 18. However, if $|V_B|$ becomes too small, the current eventually decreases so much that the ohmic losses decrease and hence $|V_S-V_B|$ starts increasing. This means that $|V_B|$ increases slightly again and settles both $|V_S-V_B|$ and i to their final asymptotic values. Hence, the same happens for P_4 and P_2.

In order to observe the same behavior on the curves of Figure 15 and Figure 16, that relate to the case of lower resistivity, we would have to go to much higher values of R_B, because this effect is critically dependent upon ohmic losses, which are now smaller.

Calculations of powers referring to configuration A (with an ion gun at the Shuttle such that $V_s \sim 0$) will not be reported here, since they leave the previous general discussion unchanged.

We report instead, in Figure 19, the power P_4 available for wave generation, versus balloon radius for the more practical case of configuration B (balloon upward) with an electron gun at the Shuttle keeping the Shuttle potential low. (The calculation refers to ρ = 0.03μΩm.) The values of power are substantial: above 10 kilowatts up to $R_B \sim 3$ m. They then decrease with radius on account of the high currents (see Figure 9) and the correspondingly high ohmic losses, but still remain substantial for the radii considered.

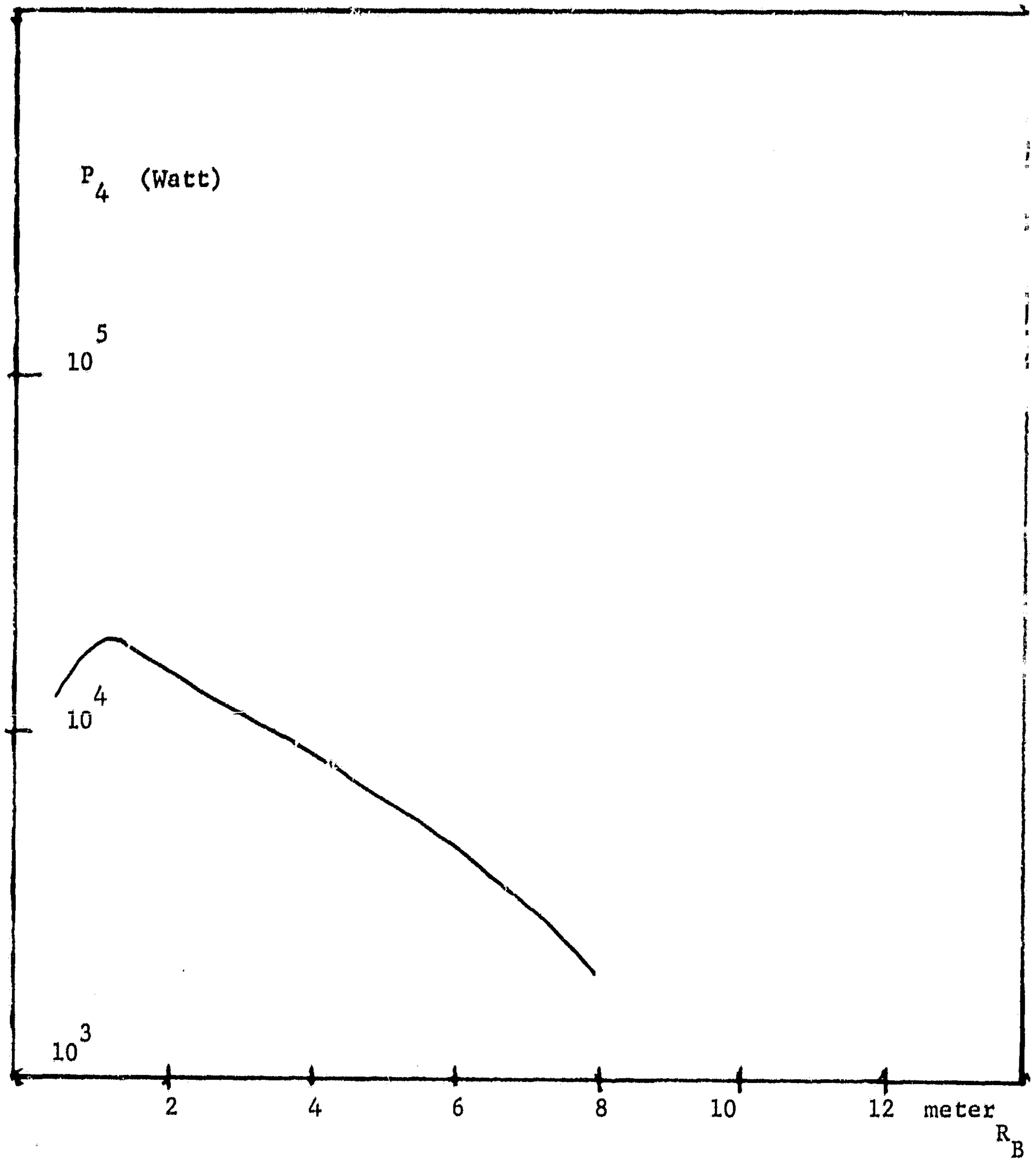

Figure 19. Power level P_4 available for e.m. wave generation; Configuration B, L = 100 Km , ρ =0.03 $\mu\Omega$m , r_W = 0.5 mm ; electron gun onboard the Shuttle, so that $V_S \cong 0$.

3. Effects of Accelerated Secondary Electrons

3.1 Introduction

The investigation of possible processes generated by accelerated secondary electrons poses a difficult problem. It requires, first of all, an investigation of electron trajectories in the sheath region surrounding the balloon, to determine their distributive function outside this region. Second, one has to investigate the stability of such distributions in the background plasma with respect to the generation of electromagnetic waves, and actually go to the non-linear stage of instability in order to be able to calculate the efficiency of these processes. A final problem concerns those high-energy electrons that have possibly survived any of these interactions: we must evaluate their energy degradation in the atmosphere and the possible resulting excitation of luminous phenomena. We will not go into all these detailed mechanisms here. Consistent with the rest of the report, however, we will outline the various phenomena involved to get an idea of their possible relevance for future studies.

3.2 Distribution of Secondary Electrons

As we have already metioned (see Section 2.4), one may suppose that the sheath electric field around the balloon is radial and, in order of magnitude, given by:

$$E \sim V_B / R_{\text{sheath}}$$

Values of the sheath thickness R_{sh} have been given for various balloon radii in Table 1 of Section 2.4. If we consider the electron equation of motion in the sheath region:

$$m_e \frac{dv}{dt} = e \, [\underline{E} + \underline{v} \times \underline{B}] \tag{3.1}$$

and compare electrical and magnetic force (as we have done for the ions in Section 2.4), we are led to define the parameter:

$$\alpha^{(e)} = \frac{E}{v_{max} B} \tag{3.2}$$

with:

$$\frac{1}{2} m_e v_{max}^2 = eV_B$$

It is:

$$\alpha^{(e)} \sim 5.62 \times 10^{-2} \left(\frac{V_B}{R_{sh}}\right)^{1/2} \tag{3.3}$$

and we have reported values of this parameter, for various radii R_B, in Table II, having used for V_B the results of Figure 3. Contrary to the ion case, it is $\alpha_e \lesssim 1$. This means we cannot assume that the electric force is dominating. In Figure 20, which depicts the sheath region surrounding the balloon, we have $R_r = R_B + R_{sh}$. The electrons will exit the sheath region at radial distance $r = R$ from the balloon center and we want to have some idea of their distribution in a point on the flux tube at distance ρ from the line of force passing through the center of the balloon.

Table II

Values of the Parameter $\alpha^{(e)}$

R_B (meters)	V_B (volts)	R_{sheath} (meters)	$\alpha^{(e)}$
1	2.33×10^4	7.10	1.208
5	2.29×10^4	14.07	0.604
10	2.24×10^4	18.74	0.449
20	2.11×10^4	24.59	0.332
30	1.96×10^4	28.34	0.277
50	1.69×10^4	33.15	0.220

Within the sheath, the electrons are accelerated parallel to $\underline{B}$ by the parallel electric field component:

$$E_{\parallel} = E_R \cos\theta \qquad (3.4)$$

and, with the notation of the figure,

$$\sin\theta = \frac{\rho_1}{R_r} \qquad (3.5)$$

The velocity $v_{\parallel_o}$ (ρ), which they attain after tranversing the sheath under the accelerating force, is given by:

$$V_{\parallel o}(\rho) = \sqrt{2}\,\left(\frac{eV_B}{m_e}\right)^{1/2} \left(1 - \frac{\rho_1^2}{R_r^2}\right)^{1/4} \qquad (3.6)$$

It tends to 0 for $\frac{\rho_1}{R_r} \to 1$, such as on the boundary of the flux tube; the electric field (radial) tends to be perpendicular to $\underline{B}$.

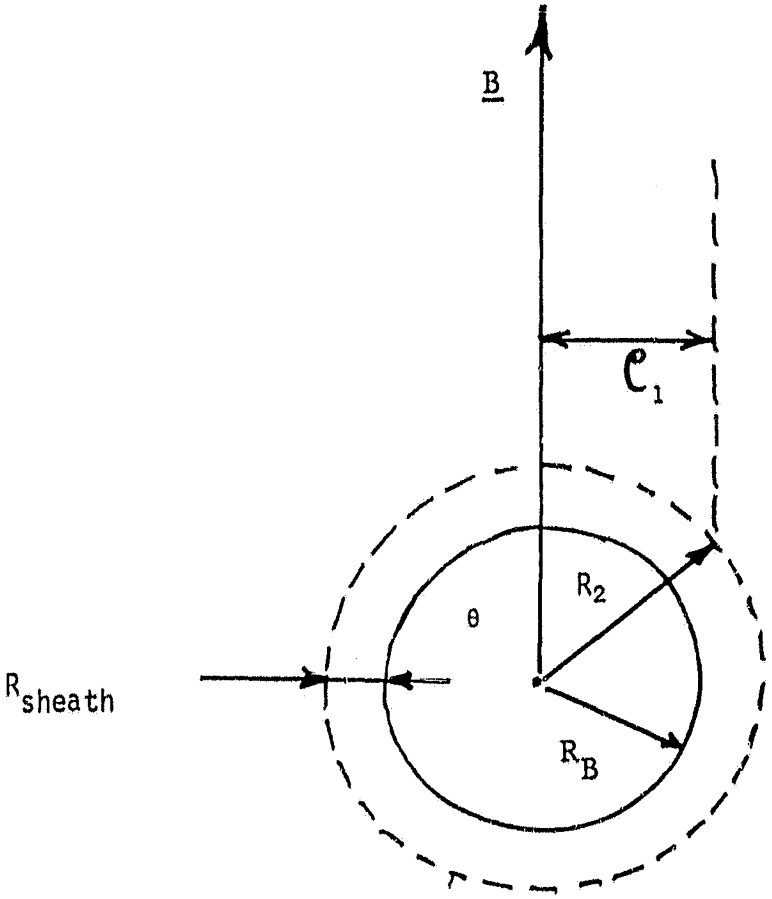

Figure 20. Geometry of the sheath region surrounding the balloon

The motion perpendicular to $\underline{B}$ is, to a good approximation (as the electron Larmor radius R_e is << R_{sh}), given by the $\underline{E} \times \underline{B}$ drift and the corresponding perpendicular velocity is:

$$v_{\perp o}(\rho) = \frac{E_\perp}{B} \sim \frac{1}{B}\frac{V_B}{R_{sh}}\;\frac{\rho_\perp}{R_r} \qquad (3.7)$$

This tends to 0 as $\frac{\rho_\perp}{R_r} \rightarrow 0$, while the electric field tends to become parallel to $\underline{B}$. The electron distribution function then can be written, for example, as:

$$f(\rho, v_\perp\ v_\parallel) = n_b(\rho)\exp\left\{-\left(\frac{v_\parallel - v_{\parallel o}(\rho)}{v_{the}}\right)^2 - \left(\frac{v_\perp - v_{\perp o}(\rho_\perp)^2}{v_{the}}\right)\right\} \qquad (3.8)$$

where $n_b(\rho)$ is the density of the secondary electrons and v_{the} ($\sim 1.5 \times 10^2$ km/sec) their small thermal velocity.

3.3 Electromagnetic Instabilities of Secondary Electron Beams

To be excited, all electromagnetic modes require an excess of perpendicular (over parallel) momentum (Melrose 1973, Mangeney and Veltri 1976). A practical condition for any of the electromagnetic instabilities is that:

$$y = \text{arct}\,\frac{v_{\perp o}}{v_{\parallel o}} < 25° \qquad (3.9)$$

If we express this condition using the above formulae (3.6) and (3.7) for $v_{\parallel o}$ and $v_{\perp o}$, we obtain:

$$\frac{\rho_\perp}{R_r} > 0.955 \qquad (3.10)$$

or, equivalently, for the angle θ of Figure 2, $\theta > 73°$. Therefore, possible electromagnetic instabilities are expected only quite close to the boundaries of the flux tube cut through by the balloon.

Next, we will briefly discuss the type of electromagnetic instabilities we have to expect. Let's look just at the cyclotron resonance condition:

$$\omega - \nu\Omega_{ce} \sim n\omega\cos\theta \frac{v_{\parallel}}{c} \sim 0 \qquad (3.11)$$

with $n = \frac{kc}{\omega}$ the index of refraction, θ being now the angle between $\underline{k}$ and $\underline{B}$ and $\nu = 0, \pm 1, \pm 2$, etc. For the ionospheric condition:

$$\frac{\omega_{pe}}{\Omega_{ce}} \sim 10 \qquad (3.12)$$

the high frequency modes (ordinary and extraordinary modes with $\omega > \omega_{pe}$ and $n < 1$) will be in resonance only for $\nu \gg 1$ and, correspondingly, have very reduced growth. The only significant instability of electromagnetic waves that would remain is that of the whistler mode at $\omega \lesssim \Omega_{ce}$.

3.4 Significance of Instabilities and Generation of UV Emissions

Condition (3.8), limiting the generation of whistler waves to the boundary of the flux tube cut through by the balloon, is quite restrictive. If we take the total power in accelerated secondary electrons (see Section 2.8) and take into account the tiny fraction of the flux tube cross-section that is significant for whistler wave generation, it is easy to see that the available power is reduced to insignificant levels. We could, therefore, conclude that electromagnetic wave emissions from secondary electrons are probably not of importance.

On the other hand, if we consider the electrons in the remaining part of the flux tube cut through by the balloon and, in particular, close to the center (which tend to have an excess in parallel velocity), it is conceivable that they might excite an instability of electrostatic plasma waves. A quantitative appreciation of this effect could be a topic for future studies.

In the same way, it would be worthwhile to investigate the possibility that accelerated electrons, in the absence of other interactions, reach the earth's atmosphere and finally lead to the excitation of some luminous phenomena (for example, excitation of UV radiation). An appreciation of this possibility comes indirectly from a comparison with the observation of Lyman α UV excitation at the foot of the flux tube of Jupiter's satellite Io from the Copernicus telescope (Atreya et al., 1977). These authors estimate that the interaction of keV electrons of 100 ergs $cm^{-2}sec^{-1}$ with the Jovian upper atmosphere produces approximately 100 kR (kiloroengten) of hydrogen Lyman-α at each foot of Io's flux tube.

In our case, from Figure 18, we have for $R_B = 5m$:

$$P_3 \sim 2.5 \times 10^3 \text{ watts}$$

and correspondingly, a power density:

$$PD \sim 3 \times 10^4 \text{ ergs } cm^{-2}sec^{-1}$$

Although this is an overestimate (and we also have to take into account other possible losses due to instability excitation), the number obtained is above the value quoted by Atreya et al. (1977). A comparison with Io suggests, therefore, that in the case of downward deployment of the balloon, we can expect to see UV excitation at each foot of the balloon's flux tube in the earth's ionosphere. This observation will require UV instrumentation in orbit.

4. Alfvèn Wings

4.1 Discussion of the Electromagnetic Disturbance Associated with TSS

The concept of Alfvèn wings was introduced in the earlier study by Drell et al. (1965). It has gained recent experimental support from the Voyager I observations of magnetic field perturbations associated with the flux tube of Io in Jupiter's magnetosphere (Ness et al., 1979) and from further work that followed the analysis of observations (Neubauer 1980). Figure 21, taken from Banks et al. (1980), gives a pictorial view of the current wings associated with a TSS moving in Earth's ionosphere. It is important to recall some basic

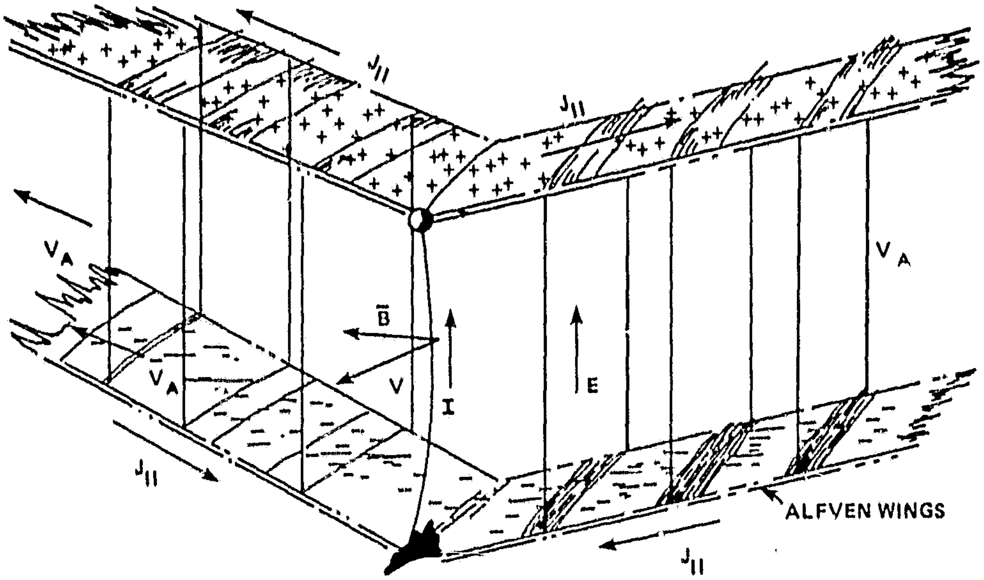

Figure 21.

Schematic view of the upper and lower current sheets which spread out from the electrodynamic tether system. The periodic darkened regions represent the outward propagation of ww frequency Alfven waves along the magnetic field. There is a net positive charge excess on the top wing and a net negative charge density on the lower wing.

(from Banks et al., 1980).

features of the disturbance associated with the TSS.

Since the ionospheric conductivity parallel to the Earth's magnetic field is extremely large at altitudes above the E layer (and much larger than the transverse conductivity), the magnetic field lines can be regarded as equipotentials. The ionospheric state is perturbed by the motion of the tether (or any large conductor) across magnetic lines. From the rest frame of the plasma one sees a polarization electric field:

$$\underline{E} = - \underline{v}_0 \times \underline{B} \tag{4.1}$$

if we refer, for the moment, to the case of a perfectly conducting tether. A corresponding potential difference is, therefore, seen between the lines of force intercepted by the ends of the system.

This perturbed state tries to readjust itself (to the previous equilibrium state, with no potential difference across field lines) through the propagation of waves from the region of disturbance (mechanism of "spontaneous" wave generation-- see Section 1.2). These waves, and associated currents parallel to $\underline{B}$ lines, are carrying away the applied potential differences, or the equivalent transverse space charge.

The problem of the electromagnetic disturbance associated with the moving tether can be formally set up as a problem of radiation from a current source (i.e., the classical problem of antenna theory). In the case of radiation in a magnetized plasma, by combining Maxwell's equations and Fourier transforming in space and time, we obtain the following equation for the space-time Fourier transform of the radiated electric field:

$$\Lambda_{ij} (\underline{k},\omega)\, E_j (\underline{k},\omega) = - \frac{4\pi i}{\omega}\, J_i{}^{o} (\underline{k},\omega) \tag{4.2}$$

where ω, $\underline{k}$ are angular frequency and wave number of the radiated waves, $\underline{J}^{o}$ represents the current source (current density) and the tensor Λ_{ij} is defined by:

$$\Lambda_{ij} (\underline{k}\omega) = n^2 (x_i x_j - \delta_{ij}) - \varepsilon_{ij} \tag{4.3}$$

with:

$$n = \frac{kc}{\omega} \tag{4.4}$$

the refraction index, $\underline{x} = \frac{k}{|k|}$ and ε_{ij} $(\underline{k},\omega)$ being the dielectric tensor of the magnetized plasma. As Stix calculated (1962):

$$\Lambda = \det \Lambda_{ij} = 0 \tag{4.5}$$

gives the wave dispersion relation.

For an observer at rest with respect to magnetic flux tubes, the tether represents a moving current source, so that we can write for the current density:

$$\underline{J}^{o} = \underline{J}^{o}\ (x,\ y - v_o t,\ z) \tag{4.6}$$

(For motion in the y direction, see Figure 22.) Consequently, by Fourier transforming in space and time and by substituting into (3.1), we obtain:

$$\Lambda_{ij}\ (\underline{k},\omega)\ E_j\ (\underline{k},\omega) = -\frac{i}{\omega}\,\delta\ (\omega - k_y v_o)\ J_i^o\ (\underline{k}) \tag{4.7}$$

The purpose of writing this equation is to point out that it constrains the angular frequency of the radiated waves, which must satisfy:

$$\omega = k_y v_o \tag{4.8}$$

This does not, of course, fix the frequency that depends upon k_y, which, in turn, depends upon the function $\underline{J}^o$ $(\underline{k})$ and upon the role played by the plasma dispersion in solution (3.7).

It is quite natural to estimate:

$$k_y \sim \frac{2\pi}{d_y} \tag{4.9}$$

where d_y is the conductor's dimension in the direction of motion. This then gives a frequency:

$$f^* = \frac{v_o}{d_y} \tag{4.10}$$

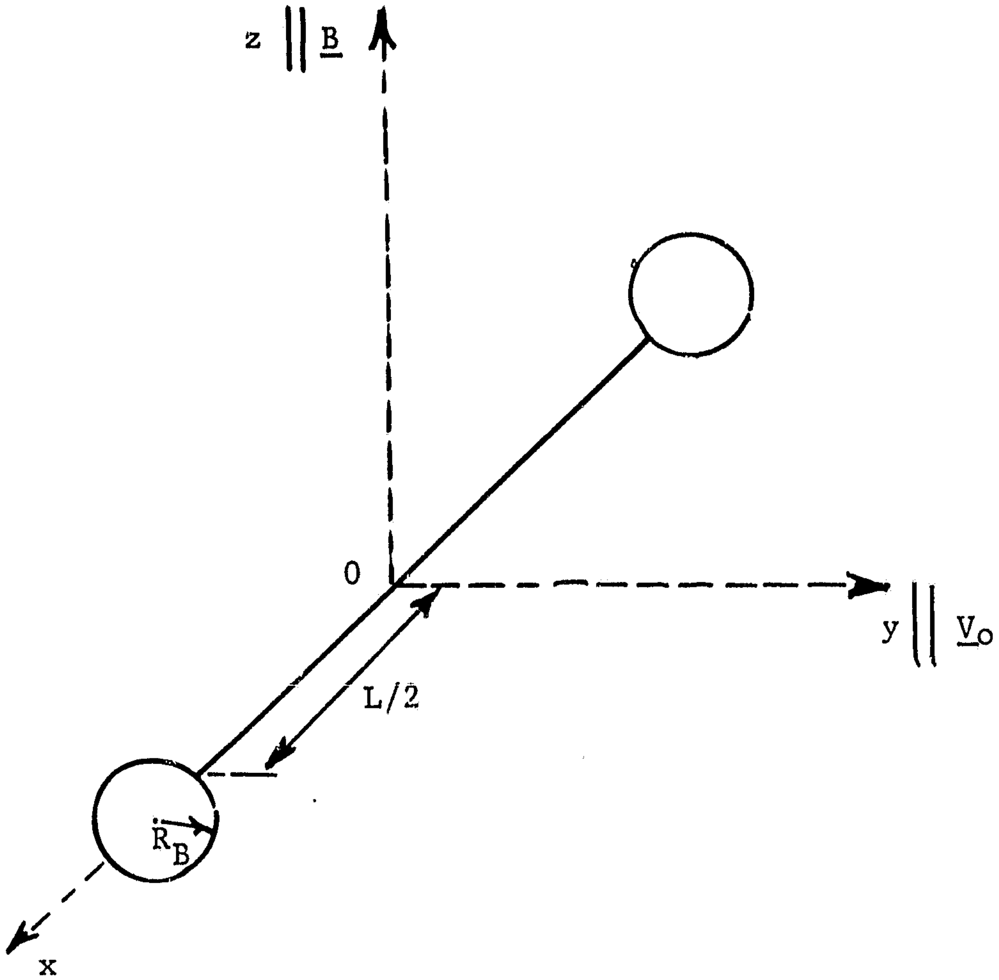

Figure 22 . Geometry of the tether-balloon system.

It is important, however, to realize that this is not the typical frequency of the electromagnetic disturbance, but rather must be interpreted as an upper limit to the frequencies contained in such disturbance. This is equivalent to saying that, for an observation site on a magnetic flux tube, the disturbance contains all frequecies:

$$f = \frac{\omega}{2\pi} < f^* \qquad (4.11)$$

while the power radiated in frequencies $f \gg f^*$ will be negligible.

Only if:

$$f^* < f_{ci}$$

as it is the case for Io, does all the power of the disturbance go into hydromagnetic waves and, in particular, into Alfvèn waves, which are then guided along magnetic lines.

In the case of the TSS, this can occur for the disturbance associated with the balloon if its radius R_B is greater than a critical value R_B^*:

$$R_B \gtrsim R_B^* \sim (20 \sin\alpha) \text{ meters} \qquad (4.12)$$

where α is the angle between velocity and magnetic field. If we refer now to the tether's cross-section ($d_y \sim 1\text{mm}$), the frequency ω^*, on the other hand, is:

$$f^*_{tether} \sim 7.8 \times 10^6 \sin\alpha \text{ Hz} \qquad (4.13)$$

Thus, the overall disturbance associated with the TSS will generally contain frequencies up into the Megahertz range. Of these wave components, only the low frequency Alfvèn waves strictly propagate their energy (at a velocity v_A) within the related magnetic flux tubes. The higher frequency components of the disturbance have different dispersion properties (Stix 1962).

4.2 Parallel Current Associated with Alfvèn Waves

The coupling of the tether's system with the plasma medium and, possibly, with the lower layers of the ionosphere, occurs through the radiation of waves. In particular, if a curent $J_{\parallel}$, parallel to magnetic field lines, is associated with these waves, it continues the tether current into the ionosphere-- down to E layer altitudes where perpendicular current closure can take place.

This parallel wave current is beyond the so-called "dc current model" of Io, proposed by Goldreich and Lynden-Bell (1969). According to the model, the flux tube intercepted by Io would actually be frozen to the satellite and follow its motion around Jupiter, with up-going and down-going parallel currents at the boundaries of the tube (the Alfvènic currents) and circuit closure-- within Io on one side, and across Jupiter's ionosphere on the other side.

We will now derive a general equation, with no approximation of small amplitude for the waves, for the parallel current associated with Alfvèn waves. The Alfvèn waves characteristics are given by (Jeffrey and Taniuti 1964):

$$\underline{v} \pm \frac{\underline{B}}{(\mu_o \rho_p)^{1/2}} = \text{constant} \tag{4.14}$$

where $\underline{v}$ and $\underline{B}$ refer to the fluctuations of velocity and magnetic field in the waves and ρ_p is the plasma mass density. The constant can be evaluated from the background properties of the plasma. In the rest frame of the plasma, then:

$$\underline{v} \pm \frac{\underline{B}}{(\mu_o \rho_p)^{1/2}} = \underline{v}_A = \frac{\underline{B}_o}{(\mu_o \rho_p)^{1/2}} \tag{4.15}$$

with $\underline{B}_o$ the earth's magnetic field.

For infinite conductivity along magnetic lines, we have:

$$E_{\parallel} = 0 \tag{4.16}$$

and Ohm's law reduces to:

$$E_{\perp} + \underline{v} \times \underline{B} = 0 \tag{4.17}$$

Taking now the divergence of this equation and combining with (4.15), it is easy to arrive at:

$$\nabla_{\perp} \cdot E_{\perp} = \mu_0 v_A J_{\parallel} \tag{4.18}$$

which relates the space charge, or potential difference, across field lines with the parallel current associated with the waves. (In our problem, space charge corresponds to the electromotive force applied by the tether between different field lines.)

On the other hand, by combining Maxwell's equations:

$$\nabla \times \underline{E} = - \frac{\partial \underline{B}}{\partial t}$$

$$\nabla \times \underline{B} = \mu_0 \underline{J}$$

we arrive at:

$$\nabla\nabla \cdot \underline{E} - \nabla^2 E = \mu_0 \frac{\partial \underline{J}}{\partial t} \tag{4.19}$$

projecting along the magnetic field (z) direction and taking into account:

$$\frac{\partial}{\partial t} (\nabla_{\perp} \cdot E_{\perp}) = \mu_0 \frac{\partial J_z}{\partial t} \quad . \tag{4.20}$$

Combining (4.20) with (4.18), we can write, for example:

$$\frac{\partial}{\partial t} (\nabla_{\perp} \cdot E_{\perp}) = v_A \frac{\partial}{\partial z} (\nabla_{\perp} \cdot E_{\perp}) \tag{4.21}$$

which tells us that the transverse space charge propagates at the Alfven speed, within the MDH framework and parallel to magnetic field lines. We will not apply these formulas to the tether-balloon system. Since the tether is itself covered by an insulator, the outside current flows only along the flux tubes cut through by the balloon and the Shuttle (*). To have an Alfvènic disturbance, we must refer to large balloon dimensions as indicated by (4.12). Then, supposing that the current is uniformly distributed across the balloon flux tube, we can write:

$$J_{\parallel} = \frac{I_{AW}}{\pi R_B^2} \tag{4.22}$$

and, from (4.13) we obtain:

$$I_{AW} \sim \frac{\pi}{2} R_B \frac{1}{\mu_o v_A} E_{\perp} \tag{4.23}$$

The perpendicular electric field, taking ohmic losses in the tether into account, is given by:

$$E_{\perp} = E_{\perp o} - \frac{R_w I_{AW}}{L} \tag{4.24}$$

where $E_{\perp o}$ is the total Lorentz field and (for motion perpendicular to $\underline{B}$):

$$E_{\perp o} = v_o B = 0.23 \text{ volt/m} \tag{4.25}$$

R_w is the tether's resistance and L is its length. Thus, we can write:

$$I_{AW} = \frac{I_o}{1 + \frac{\pi}{2} \frac{R_B}{L} \frac{R_w}{\mu_o v_A}} \tag{4.26}$$

where:

$$I_o = \frac{\pi}{2} R_B \frac{1}{\mu_o v_A} E_{\perp o} \tag{4.27}$$

is the total parallel current in Alfvèn waves, which one would have for a perfectly conducting tether.

(*) Actually, the Alfvenic current flows at an angle θ_A with respect to field lines given by $\theta_A = \arctan \frac{v_o}{v_A}$. In this case it is $\theta_A \sim 0.55°$ and is not important for the following estimates.

Figure 23 reproduces the Alfvènic current I_{Aw} as a function of balloon radius for a tether length L = 100 km and the two values of resistivity ρ = 0.03μΩm and ρ = 0.15μΩm. We have taken v_A = 800 km/sec as an average value for the Alfvèn speed between 100 and 300 km of altitude. Note that the curves are really valid only for balloon radii $R_B \gtrsim 20 \sin\alpha$ (meters), according to (4.12), as the current calculated I_{Aw} refers to waves in the hydromagnetic range of frequencies. We see from Figure 23 that the resistive limits to the current (i_R = 6.21 amps and i_R = 1.22 amps for the two respective resistivities) are not reached even at quite high values of the balloon radius.

4.3 Comparison of Alfvènic Current with Current Due to Charged Particle Collection

The current I_{Aw} calculated in the previous section, for the Alfvèn disturbance associated with TSS motion, should now be compared with the current I_c in the tether, which results from particle collection from the end electrodes (see Section 2.1).

Figure 24 gives the ratio I_c/I_{Aw} as a function of balloon radius, referring to a passive system, configuration A, and two values of resistivity (obtained from the results of Figures 5 and 23). Although the comparison has validity only for large balloon radii, the Alfvènic current is always greater than the collection current.

Assuming that the current in the tether system has to be carried along magnetic flux tubes through Alfvèn waves, the results of Figure 24 indicate that, for configuration A, particle collection at the electrodes determines the value of the current in the system. In other words, the current in the Alfvènic wings (or, approximately, in the flux tubes cut through by the balloon and the Shuttle) is limited to the value I_c.

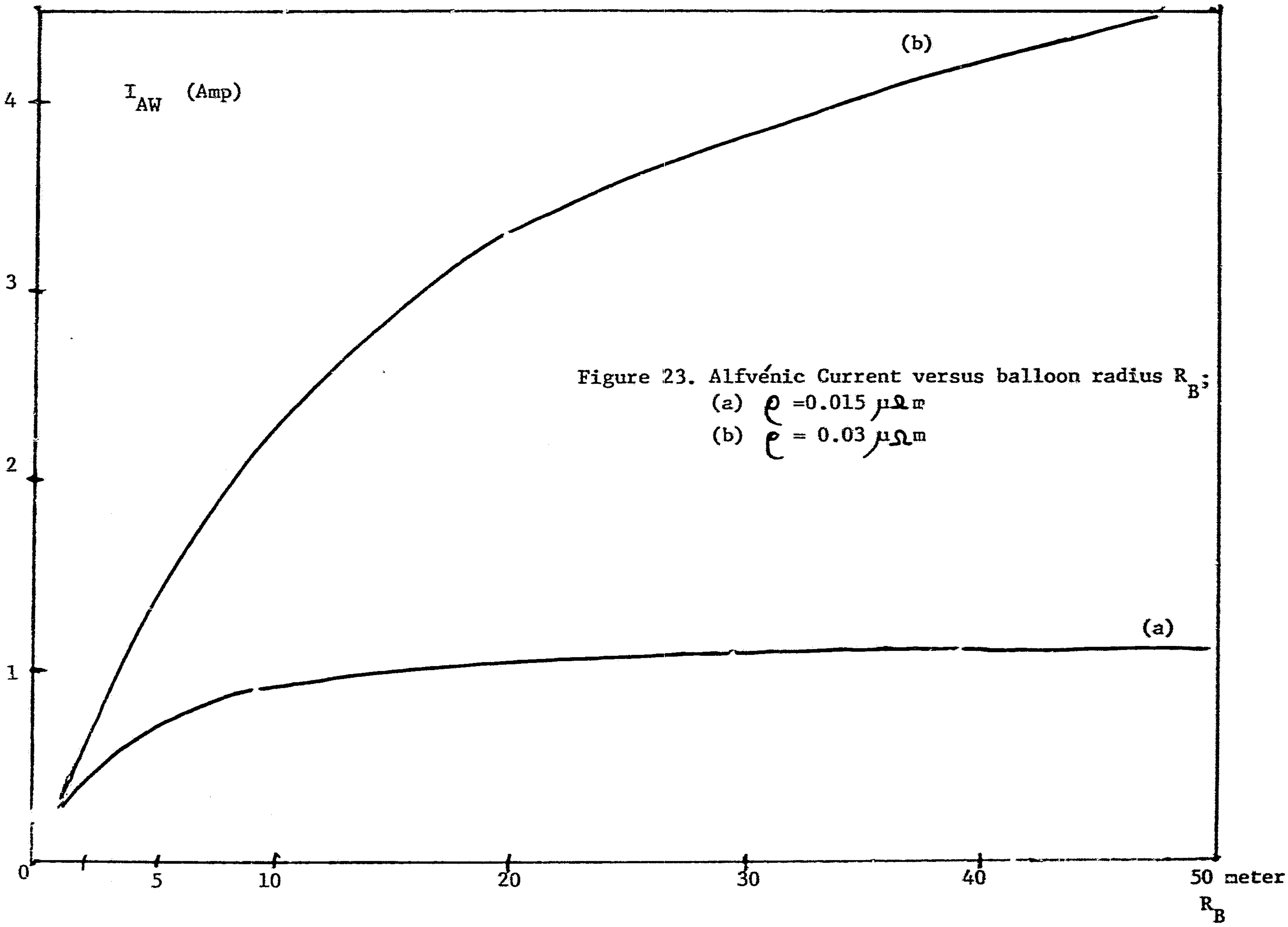

Figure 23. Alfvénic Current versus balloon radius R_B;
(a) $\rho = 0.015\ \mu\Omega m$
(b) $\rho = 0.03\ \mu\Omega m$

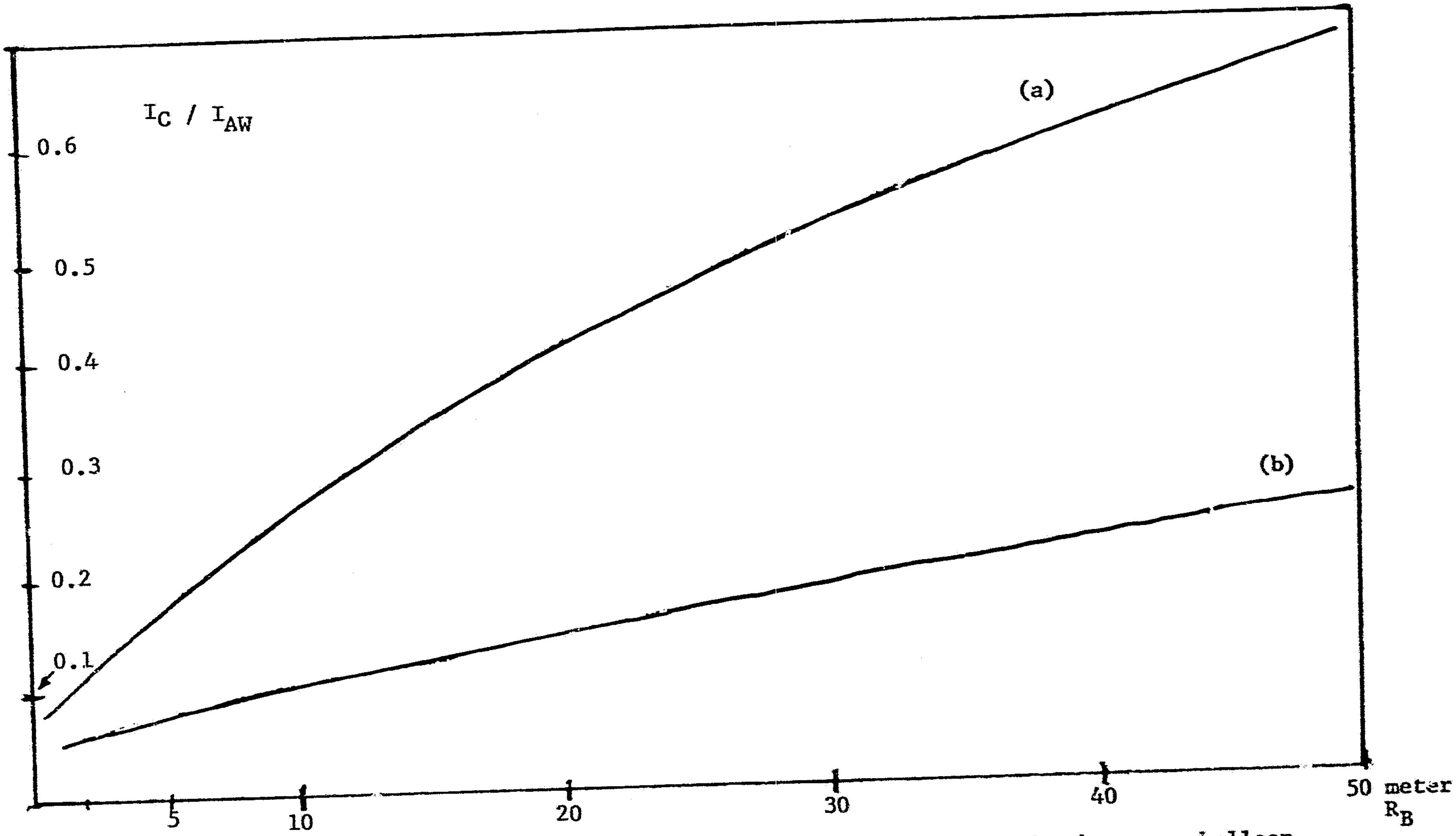

Figure 24. Ratio between collection current (I_C) and Alfvénic current (I_{AW}) versus balloon radius R_B , Configuration A; (a) $\rho = 0.15\ \mu\Omega m$; (b) $\rho = 0.03\ \mu\Omega m$.

In configuration B, and with an electron gun at the Shuttle so as to keep the Shuttle potential low, we see from Figure 9 that substantially higher values of current I_C are reached at relatively small balloon radii. We cannot compare such radii with corresponding values of I_{AW} because, in fact, we cannot speak of an Alfvènic current. There remains, however, the possibility that this case might show a limitation to the current (other than the resistive limitation), which is related to the capability of the electromagnetic disturbance produced by TSS to carry current away along magnetic lines of force.

4.4 Physical Picture of the Alfvèn Wave System Associated with TSS

When the Alfvènic disturbance in the large balloon's flux tube reaches the E layer of the ionosphere, it encounters a change in transverse conductivity. The corresponding parallel current system then closes transversally to the magnetic field through Pedersen and Hall conductivities. A result of the dense ionospheric layer is reaction to the electric field of the wave is then a possible parallel reflection of the wave electric field.

We can write:

$$E_\perp^{up} = \mathcal{R}\, E_\perp^{down} \tag{4.28}$$

where $E_\perp^{down}$ the transverse electric field of the down-going wave, $E_\perp^{up}$ is the electric field of the reflected wave, and the reflection coefficient $\mathcal{R}$ is given (Mallinckrodt and Carlson 1978) by:

$$\mathcal{R} = \frac{1 - X}{1 + X} \tag{4.29}$$

with:

$$X = \frac{\Sigma_p}{\Sigma_{AW}} = \frac{4}{\pi}\ \mu_o v_A\ \Sigma_p \tag{4.30}$$

being the ratio between the Pedersen integrated conductivity Σ_p and the Alfvèn wave conductivity ($\Sigma_{Aw} = 1/Z_{Aw}$).

If $X \gg 1$, the electric field (and therefore the $\underline{E}_\perp \times \underline{B}$ plasma velocity) is zero at the boundary. The E layer of the ionosphere acts, in this case as a metallic boundary with frozen magnetic lines. On the other hand, if $X \ll 1$, we obtain at the boundary twice the amplitude of the incoming wave. In the latter case there is negligible conductivity of the ionospheric E layer, so that in the limit of a perfectly insulating E layer, the magnetic lines have no further identity in this region.

To obtain numerical values for the reflection coefficient, we take as typical values for Σ_p (Hanson 1965):

$$\Sigma_p \sim \begin{cases} 10 \text{ mhos} & \text{at day time} \\ 3 \times 10^{-2} \text{ mhos} & \text{at night time} \end{cases} \tag{4.31}$$

Taking an average E layer altitude of h = 100 km, we can further use the following values of electron density:

$$n_e \sim \begin{cases} 2 \times 10^5 \text{ cm}^{-3} & \text{during the day} \\ 2 \times 10^3 \text{ cm}^{-3} & \text{during the night} \end{cases} \tag{4.32}$$

to determine the Alfvèn speed at the E layer. The final, typical results for the reflection coefficient R are:

$$R \sim \begin{cases} -0.92 & \text{during the day} \\ +0.17 & \text{during the night} \end{cases} \tag{4.33}$$

Thus, whereas there is almost complete reflection from the day-time ionosphere, reflection is quite weak from the night-time ionosphere, and most of the Alfvèn disturbance is transmitted further downward.

The next point to consider is the propagation time of Alfvèn waves from the tether system to the E layer levels. This time varies, of course, from one end to the other of the tether causing reflection (or partial reflection) of different parts of the wave front at different times.

Taking a typical distance of 100 km and an average Alfvèn speed of 800 km/s, we arrive at a round trip time of the Alfvèn wave:

$$\tau \sim 0.25 \text{ sec}$$

in which time the tether balloon system has moved by a distance:

$$\Delta y \sim 2 \text{ km}$$

Clearly, therefore, when there are reflected day-time waves they will no longer find the tether-balloon system on their way back from the E layer. Thus, an influence of the ionospheric E layer on the current in the tether system, which was indicated in the case of the moon of Jupiter Io (Goldreich and Lynden-Bell 1969), is not possible.

Correspondingly, the picture of a so-called "dc current circuit" moving with the tether-- i.e., a freezing with the tether's motion of the intercepted flux tubes (which would then slip with respect to the ionospheric base)-- is not appropriate.

What happens in daytime is that the Alfvèn waves radiated by the tether are partially reflected from the ionospheric E layer. They then travel back to the conjugate ionosphere, where they are again partially reflected, and the process repeats for a number of times. During its motion, the tether system generates a system of waves reflected back and forth between conjugate zones of the E layer, all along its orbit.

It is interesting to ask how many reflections are possible before the amplitude of a given wave decreases significantly. When reflections occur with the same reflection coefficient R, the number of successive reflections necessary to achieve a $\frac{1}{e}$ reduction of the wave amplitude would be:

$$N \sim \frac{\Sigma_p}{2\Sigma_A} \left(1 + \frac{1}{e}\right) \text{ for } \Sigma_p > \Sigma_A \tag{4.34}$$

Thus, $N \sim 12$ for reflections between daytime ionospheres. In the case of nighttime ionospheres ($R \sim 0.17$), more than 80% of the Alfvènic disturbance is transmitted downward.

4.5 Power into Guided Alfvèn Waves

Alfvèn waves are guided along the magnetic tubes of force, i.e., their energy is propagated along magnetic field lines. As a consequence, the power in Alfvèn waves can be obtained by multiplying the wave energy density W for the volume filled up by wave energy in a second. This volume, in turn, will be given by the cross-section of the flux tubes intercepted by the system (A) multiplied by the wave group velocity v_G.

Thus:

$$P_{AW} = W \times 2A \times v_G \tag{4.35}$$

where the factor 2 indicates wave propagation in two opposite directions with respect to the tether system (down to conjugate regions of the low ionosphere).

For Alfvèn waves, it is easy to show that:

$$W_{AW} = \frac{B^2}{2\mu_o} \tag{4.36}$$

B^2 being the magnetic field of the perturbation. That is, the energy of the fluctuations is entirely magnetic. Thus, again using $v_G = v_A$, we obtain for the power P_{AW} associated with Alfven waves:

$$P_{AW} = \frac{B^2}{\mu_o} A \, v_A \tag{4.37}$$

As it refers to Alfvèn waves, this formula is valid only for sufficiently large dimensions of the conductor in the direction of motion [see (4.12)]. For the TSS system, it will, therefore, apply to power contained in the balloon cross-section, where the balloon radius satisfies:

$$R_B \gtrsim (20 \sin\alpha) \text{ meters} \tag{4.38}$$

In terms of the flux tubes cut through by the conducting part of the Shuttle and the tether itself, the formula is not strictly applicable. This is because the corresponding electromagnetic disturbances contain components of frequencies above the hydromagnetic range, which neither have an energy density given by (4.36) nor propagate parallel to $\underline{B}$ with group velocity v_A. We will, therefore, use (4.37) to calculate the Alfvènic power specifically in the balloon flux tube.

The perturbation magnetic field in (4.37) is calculated in terms of the transverse electric field across the balloon cross-section:

$$B \sim \frac{1}{v_A} E_\perp \tag{4.39}$$

and, taking into account resistive losses in the tether:

$$E_\perp = E_{\perp o} - \frac{R_w i}{L} \tag{4.40}$$

with:

$$E_{\perp o} = v_o B_o \sin\alpha \tag{4.41}$$

Thus, we obtain for the Alfvenic power:

$$P_{AW} \sim \frac{(E_{\perp o} - R_w i)^2}{\mu_o v_A} \pi R_B^2 \tag{4.42}$$

In (4.42), referring to configuration A, we will have to use the current:

$$i = i_c(R_B)$$

due to charged particle collection (see Section 4.3).

An input impedance Z_{AW} of the balloon flux tube, with respect to guided Alfvèn waves, can now be easily calculated from:

$$Z_{AW} = \frac{\Delta V^2}{P_{AW}} \tag{4.43}$$

where:

$$\Delta V \sim 2R_B E_\perp$$

is the potential difference across the flux tube. From (4.42) and (4.43) we obtain:

$$Z_{AW} = \frac{4}{\pi} \mu_o v_A \tag{4.44}$$

A typical value of this impedance, at the altitudes of interest to us, is:

$$Z_{AW} \sim 1.3 \text{ ohms}$$

Figure 25 shows our results for the power P_{AW}, as a function of balloon radius. We are referring to configuration A, a passive system, and the two values of resistivity $\rho = 0.03\mu\Omega m$ and $\rho = 0.15\mu\Omega m$. For example, for $R_B = 40m$, we obtain:

$$P_{AW} \sim 200 \text{ watts for } \rho = 0.03\mu\Omega m$$

$$P_{AW} \sim 60 \text{ watts for } \rho = 0.15\mu\Omega m$$

The difference between the two curves, and, in particular, the knee in curve b) that refers to the case of higher resistivity, are understandable in terms of the concepts that we have already introduced and of the formula (4.42) that was used to compute P_{AW}. Curve b) reaches a plateau between $R_B \cong 50$ m and $R_B \cong 90$ m. This is due to the fact (see Figure 5) that, for the same radius, the current, and hence the ohmic losses, that appear in equation (4.42), do not vary very much. At about $R_B \cong 90$ m, the balloon potential drops to a small value (see Figure 4) and, correspondingly, the Shuttle potential increases. Hence the current start increasing again (see Figure 5), and this determines an increase in ohmic losses. This more than balances the increase of P_{AW} with R_B^2 and explains qualitatively the decrease in P_{AW} for $R_B \gtrsim 90$ m. For $R_B \gtrsim 100$ m, P_{AW} increases again. This last trend is due to the fact, already mentioned in connection with Figures 17 and 18, that for $\rho = 0.15 \mu\Omega m$ and $R_B > 100$ m, the current, and hence the ohmic losses, reach an asymptotic value.

The electric field, then (see equation 4.40), does not vary any more and we see from the same equation that P_{AW} starts increasing as R_B^2. This behavior does not appear in curve a) of Figure 25. It would appear at much higher values of R_B, not shown in the Figure, owing to the smaller value of the wire resistivity, and hence to the reduced relevance of the ohmic losses. The reader should take note that what we have calculated here is strictly the power contained in the flux tube cut through by the large balloon. The tether enters the calculation only through the ohmic reduction of the transverse electric field across the tube [see (4.40)], due to its internal resistance. This power has, therefore, nothing to do with the total power radiated by TSS as a driven antenna (if its current were pulsated) at different frequencies. It is in this last power that the radiating properties of the tether as a long dipole (and, therefore, its length) will enter in an essential way.

4.6 Preliminary Considerations on Wave Detectability on the Ground

4.6.1 General

A source of electromagnetic radiation in the ULF/ELF band, embedded in Earth's ionosphere (typical height 200 km), illuminates Earth's surface through several possible propagation mechanisms. One of them could be properly called the "artificial micropulsation" mechanism. This mechanism consists of Alfvèn waves that are guided by the lines of force of Earth's magnetic field, from satellite height to the bottom of the ionosphere, spread from there downward semi-spherically and directed to Earth's surface as horizontally polarized downward e.m. waves similar in many respects to a natural micropulsation. An estimate of the expected field intensity for this case can be formulated on the basis of the geometric optics treatment worked out by Kelly et al. (1974, 1976). This is based on the computation of the "wave-spreading factor," as illustrated in Figure 26.

A second mechanism consists in the excitation frequencies at ULF/ELF of the Earth-Ionosphere wave guide from a satellite-borne antenna. This mechanism was analyzed by Einaudi and Wait (1971a, 1971b) for the case of a flat Earth and of a vertical geomagnetic field orientation, and by Pappert (1973) for spherical Earth and arbitrary magnetic field orientation. These authors have all considered an infinitely small dipole as the satellite-borne radiator. With this second mechanism, the satellite-borne antenna excites in principle, long-range, quasi-TM and quasi-TE modes, which propagate horizontally in the Earth-Ionosphere wave guide, away from the sub-satellite point. Some of these modes are characterized by very low attenuation. However, the excitation factors involved are exceedingly small, especially for the case of the vertically polarized satellite-borne elementary dipole, which is of direct interest here.

4.6.2 Estimates of E.M. Field Intensities at Earth's Surface

By following the geometric optics approach of Kelly et al. (1974), we compute first the radiation intensity U (power per unit solid angle) of the orbiting antenna. In the case of an isotropic radiator, with output power P, we have:

$$U = \frac{P}{4\pi}$$

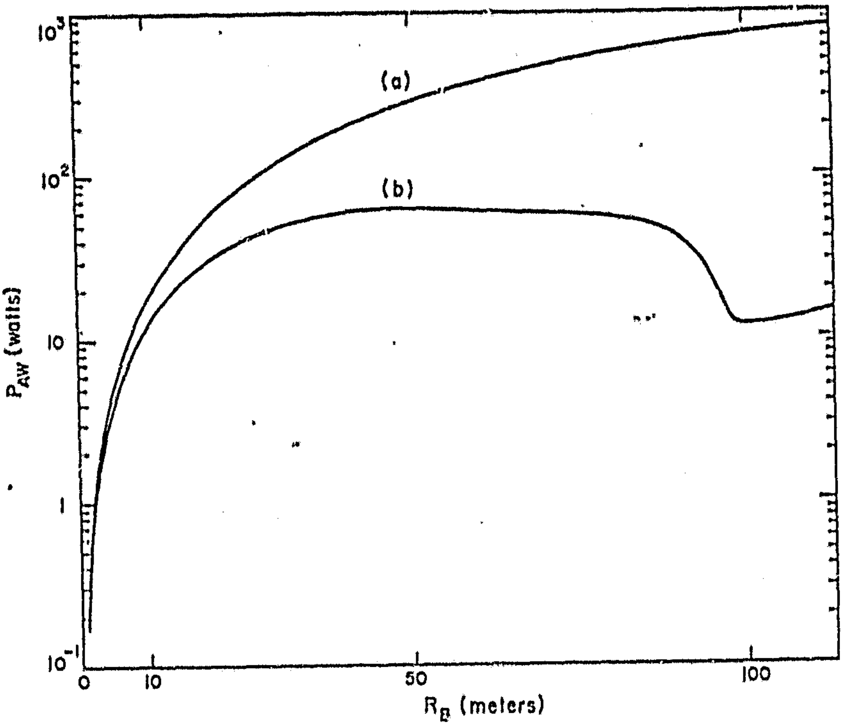

Figure 25. Power in Alfven wave from a single balloon versus balloon radius; Configuration A, (a) $\rho = 0.03\ \mu\Omega m$ (b) $\rho = 0.15\ \mu\Omega m$.

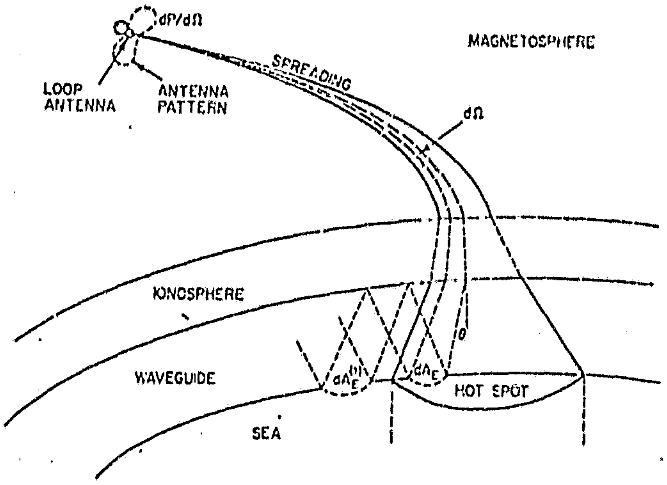

Figure 26. Spreading factor quantities $d\Omega$ and dA_E. The multihop area element $dA_E^{(1)}$ is also shown. (from Kelly et.al., 1974)

In our case, which pertains to the excitation, by the orbiting antenna, of Alfven waves, we have:

$$U = \frac{P}{2}$$

because all the power is channeled along the line of force of the geomagnetic field passing through the source, with half of the power propagating upward and half downward. The power density P_d $(\frac{\text{watts}}{m^2})$ at Earth's surface (vectors $\vec{E}$ and $\vec{H}$ are horizontal) is then obtained by multiplying the radiation intensity U by the spreading factor $\frac{1}{\cos\alpha} \frac{d\Omega}{dA_E}$ (m^{-2}), computed with the geometric optics approach:

$$P_d = U \frac{1}{\cos\alpha} \frac{d\Omega}{dA_E}$$

Examples of the computation performed by Kelly _et al_. (1974) are given in Figures 27 and 28. These two figures define the symbols used in the expression of the spreading factor and give its dependence upon latitude and longitude for the frequency of 3kHz, for two altitudes of the orbiting antenna, and for three models of the ionosphere. Model A1 is characterized by a linear increase of electron density from 70 km to 300 km, with 10^3 el/cc at 70 km and 2 x 10^5 el/cc at 300 km. Model A2 is characterized by a realistic profile of the bottom-side ionosphere, with 10^3 el/cc at 84 km, 10^4 el/cc at 200 km, and 2 x 10^5 el/cc at 300 km. Model A3 is characterized by a latitudinal dependence and by a smoothly varying electron density with height. All these models are described in the Appendix to Kelly _et al_. (1974).

In order to compute, without performing ray tracing, the spreading factor at frequencies in the ELF/ULF band, other than the VLF ones chosen by Kelly _et al_. (1974) in their examples, the following approximate equality can be used:

$$\text{spreading factor} = \frac{1}{\cos\alpha}\frac{d\Omega}{dA_E} \cong \frac{1}{\mu^2 h^2}$$

where μ is the index of refraction of the wave at satellite height and h is the height of the bottom of the ionosphere above ground. Table III taken from Kelly et al. (1974) compares rigorous and approximate calculation of the spreading factor, for the frequency of 3kHz, for several satellite heights, for various latitudes and for three ionospheric models.

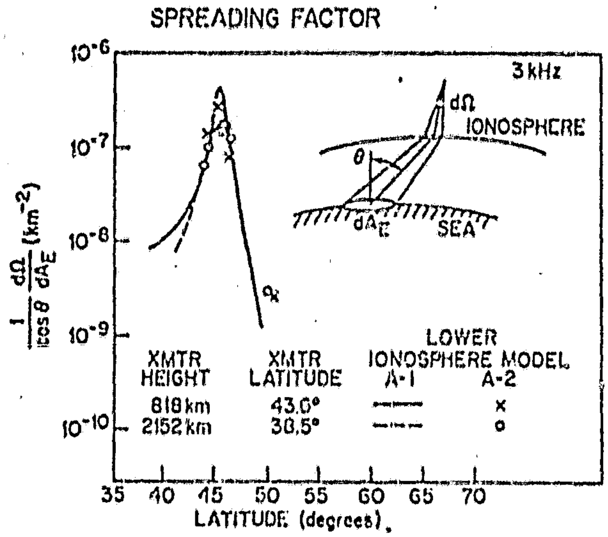

Figure 27.

Variation of spreading factor with receiver latitude for two fixed transmitter locations. The X's and O's are results for lower ionospheric Model A-2. The lines are results for Model A-1 (from Kelly et al., 1974).

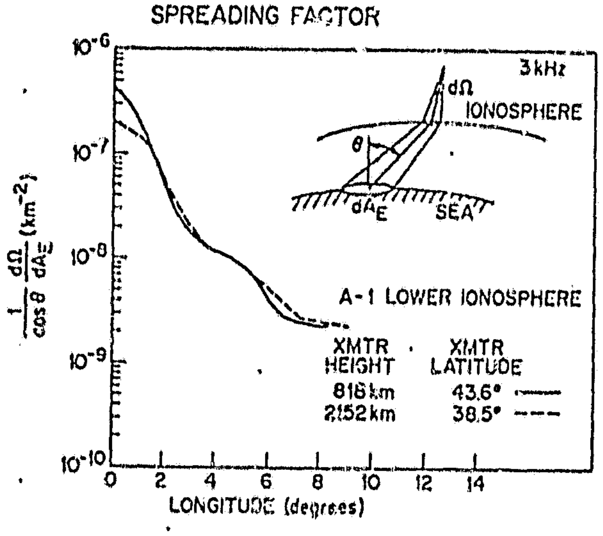

Figure 28.

Variation of spreading factor with receiver longitude for two fixed transmitter locations. Model A-1 results are shown (from Kelly et al., 1974).

Table III

Comparison of the 3-kHz spreading factor obtained by geometric optics calculation $(\frac{1}{\cos\alpha}\frac{d\Omega}{dA_E})$, with the approximate value $(\frac{1}{\mu^2h^2})$.

Transmitter Coordinates Height (km), Latitude		Lower Ionosphere Model	Approximate Value* $\frac{1}{\mu^2h^2}$ (km^{-2})	Geometrics Optics Expression $\frac{1}{\cos\alpha}\frac{d\Omega}{dA_E}$ (km^{-2})
818	43.6°N	A-1	6.8×10^{-7}	4.3×10^{-7}
818	43.6°N	A-2	4.7×10^{-7}	2.8×10^{-7}
818	43.6°N	A-3	4.6×10^{-7}	1.77×10^{-6}
2152	38.5°N	A-1	8.95×10^{-7}	2.0×10^{-7}
2152	38.5°N	A-2	6.21×10^{-7}	1.6×10^{-7}

* For comparisons to ray-tracing prediction using Models A-1, A-2 and A-3, heights h of 70, 84, and 70 km, respectively, in the expression $\frac{1}{\mu^2h^2}$. (Ionospheric Models A1, A2, A3, as described in the Appendix to Kelly et al., 1974).

Table III shows that, at least for the computation conditions adopted, the approximate value of the spreading factor is accurate enough the for purpose of our study. By assuming that the accuracy of the expression $\frac{1}{\mu^2 h^2}$ for the spreading factor holds true at ULF/ELF frequencies, we have the following value of power density at Earth's surface and at the frequencies of interest:

$$P_d = \frac{P}{2} \cdot \frac{1}{\mu^2 h^2}$$

where P is assumed to be 100 watts.

$\mu = \frac{c}{v}$, with c = velocity of light in free space = 3×10^8 m/sec

v = velocity of Alfvèn waves = 8×10^5 m/sec

h = height of ionospheric bottom above Earth's surface = 6×10^4 m

Therefore:

$$P_d = \frac{100}{2} \frac{1}{(375)^2\ (6 \times 10^4)^2} = 1.6 \times 10^{-13}\ \text{watts/m}^2$$

and $H_s = 1.62 \times 10^{-8}\ \frac{\text{At}}{\text{m}}$ (-156 db with respect to $\frac{1\text{At}}{\text{m}}$).

$E_s = 6.14 \times 10^{-6}\ \frac{\text{V}}{\text{m}}$ (-104 db wrt $\frac{1\text{v}}{\text{m}}$)

(both $\vec{H}_s$ and $\vec{E}_s$ are horizontally polarized).

The noise levels that the signal has to overcome are:

- internal noise of a cryogenic magnetometer, $H_N = 7.9 \times 10^{-9}$ At/m (-162 db/$\sqrt{\text{Hz}}$ with respect to $\frac{1\text{At}}{\text{m}}$; this is -172 db wrt $\frac{1\text{At}}{\text{m}}$ when using 0.1 Hz bandwidth)
- external micropulsation noise (discontinuous occurrence) $H_N = 7.9 \times 10^{-8}\ \frac{\text{At}}{\text{m}}$ (-142 db/$\sqrt{\text{Hz}}$ wrt $\frac{1\text{At}}{\text{m}}$), for horizontally polarized H_N. This is -152 db wrt $\frac{1\text{At}}{\text{m}}$, when using 0.1 Hz bandwidth).

Therefore, the signal-to-noise ratio is approximately +16 db (in 0.1 Hz band-width) in the time intervals during which micropolarization activity (for instance, "pearls," with carriers at a few Hertz) subsides, and the only noise to contend with it the cryogenic magnetometer's internal noise. On the contrary, the signal-to-noise ratio (SNR) is approximately -4 db (still in 0.1 Hz bandwidth) when micropulsation activity occurs. We think that this is adequate enough for an initial experiment, considering that micropulsation activity in the frequency band of interests (ELF/ULF) is a discontinuous phenomena. Besides, in such a case as natural "pearls," the trains are made of bursts (for instance, of 1 c/s carrier) alternating with pauses, which makes it possible to detect the satellite-emitted signals even with an SNR as low as -4 db. Signal integration with longer integration times would further enhance detectability.

Let's consider now the case of the excitation of quasi-TM and quasi-TE guided modes in the Earth-ionosphere cavity, due to an infinitesimally small elementary dipole in orbit. Limiting ourselves to an example with a carrier frequency of 75Hz (the frequency of the numerical example worked out by Pappert, 1973), we have the same field intensities as Pappert if we choose an orbiting antenna 318 km long, with a current of 10 amp (electric moment = 3.18×10^6 Am). The signal intensities to be expected at Earth's surface can be read in this case along the y-axis scale, which is to the left in Figure 29 and along Earth's surface of several megameters from the vertical that contains the orbiting radiator. However, the tether antenna presently under consideration by the designers of the TSS facility has a length of 100 km. If the current acquires the realistic value of 1.79A (electric moment = 1.79×10^5 Am), the signal intensities are expected to be smaller. Their values can be found by changing, in Figure 29 and Figure 30, the scale of

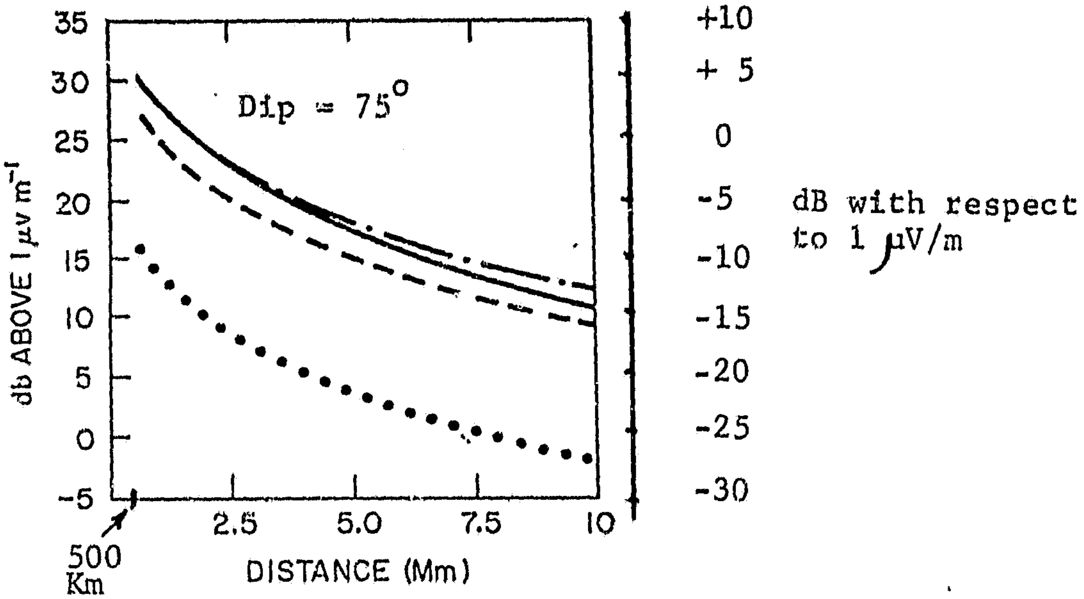

NOTE

Dip is at 0° at the magnetic equator

Figure 29

Signal levels versus distance. Signal levels for electric-dipole sources referred to a current moment of 3.18×10^{6} amp-m. Signal levels for magnetic dipole sources referred to a current loop of 2.02×10^{14} amp-m². The azimuth is 90°, the dip is 75°; and the frequency is 75 Hz. Legend: — — — — ground-based electric dipole, end fire, $\sigma = 10^{-4}$ mho m^{-1}; • • • • • • vertical electric dipole, 500 km; ———— horizontal electric dipole, broadside and end fire, 500 km; ——•—— horizontal magnetic dipi broadside and end fire, 500 km.

(from Pappert, 1973).

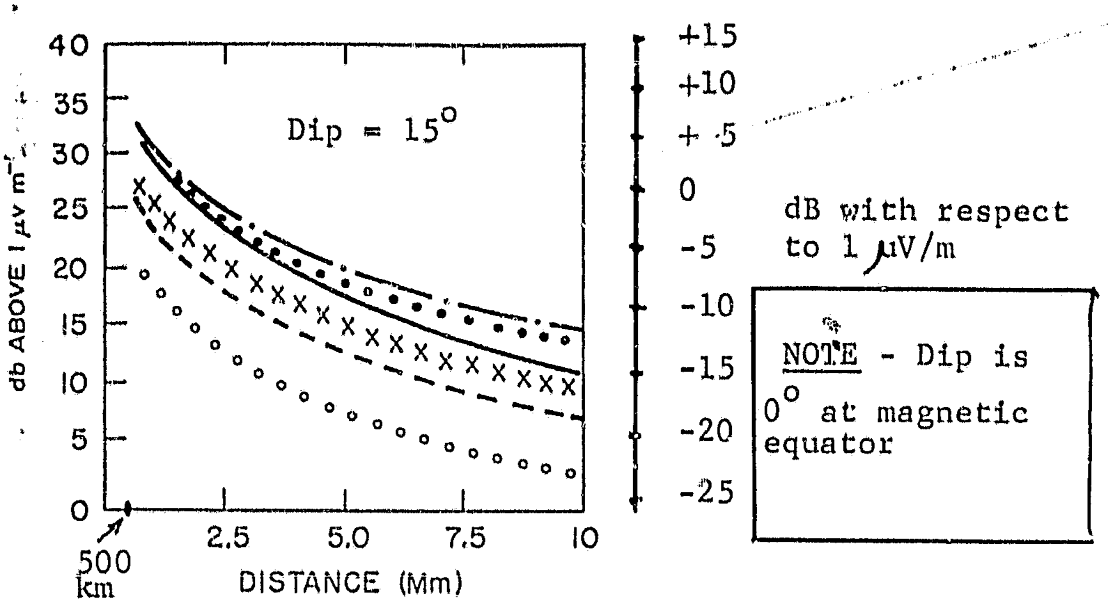

Figure 30

Signal levels versus distance. Signal levels for electric-dipole sources referred to a current moment of $3.18\ 10^6$ amp.m. Signal levels for magnetic dipole sources referred to a current loop of $2.02\ 10^{10}$ amp.m^2. The azimuth is 90°, the dip is 15°, and the frequency is 75 Hz. Legend : — — — — ground-based electric dipole end fire, $\sigma = 10^{-4}$ mhos/m; • • • • • • • vertical electric dipole, 500 Km; ———— horizontal electric dipole, end fire, 500 Km ; o o o o o o o o horizontal electric dipole, broadside, 500 Km ; X X X X X horizontal magnetic dipole, end fire, 500 Km; ——·——· horizontal magnetic dipole, broadside, 500 Km.
(from Pappert, 1973)

the y axis from the one on the left side (Pappert, 1973) to the one on the right side. This decrease of the electric moment causes, in fact, a 25 db decrease in signal intensity. Figure 29 indicates that for a dip of 75°, and at a distance of 500 km (along the surface of Earth) from the vertical that contains the satellite (elementary dipole, vertically oriented, at a height of 500 km above Earth's surface), the signal intensity is approximately -7.5 db wrt $\frac{1\mu V}{m}$ (= 0.42 $\frac{\mu V}{m}$). Under the same conditions, except with the dip = 15°, Figure 30 gives a signal intensity of +7.5 db wrt $\frac{1\mu V}{m}$ (= 2.38 $\frac{\mu V}{m}$). If we observe with a cryogenic magnetometer the horizontally polarized magnetic field of the wave (integration time adopted = 10 seconds, as before), we have a SNR that varies between +8 db and -7db for a dip inclination's change from 15° to 75°. This assumes that the only noise we have to contend with is the cryogenic magnetometer's internal noise.

It would appear that the illumination of a "hot spot" (Kelly et al., 1974) on Earth's surface, by simulating an artifical micropulsation, is a more favorable mechanism (at least at close range from the vertical that contains the orbiting radiator) than the excitation of quasi-TM or quasi-TE, long-range, guided modes in the Earth-ionosphere cavity.

This conclusion holds for the case in which the model adopted for the orbiting radiator is an infinitesimally small elementary dipole, (but it is characterized by the total moment of the long wire), and is vertically oriented. We recommend possible follow-on efforts that adopt the more realistic, albeit more complex, model of an orbiting antenna with its full length (100 km or larger).

5. Conclusions

The report has investigated the potential capability of the electrodynamic tether to generate electromagnetic waves in the ionospheric plasma. We presented several results concerning current-voltage characteristics of the tether. It has been pointed out that, in a purely passive configuration--either with the tether deployed downward or upward, relatively large potentials may develop at the Shuttle. To avoid this, one should consider using charged particle guns. The calculations have included the effect of secondary electron emission from the balloon surface, which can be significant for configuration A when the balloon is at high potentials with respect to the plasma. The final scope of these calculations indicates the possibility of having large currents in the tether and of computing, correspondingly, the power dissipated in ohmic losses, the power going possibly into accelerating secondary electrons, and the remaining electrodynamic power that is, in principle, available for wave generation.

An important conclusion is that significant powers are available for wave generation, even when effects of secondary electrons are taken into account (and in the framework of an overestimation of that effect). For configuration A (tether deployed downwards), we find powers of the order of some kilowatts even for balloon radii as small as $\sim$5 meters, and greater for larger balloon radii. For configuration B (tether deployed upwards), if one uses an electron gun at the Shuttle in such a way as to keep it at plasma potential, one obtains both large currents and correspondingly large powers for wave generation at very small radii. For example, for $R_B = 2$ meters, the current is $i \sim 4$ amps and the power is above 10^4 watts.

In the case of a particular electrodynamic phenomenon and a program for observing it, (either from a sub-satellite in the ionosphere or from the ground,) the above calculations of current-voltage characteristics constitute the basis on which to decide what parameters of the TSS system are necessary to make that phenomenon detectable.

A consideration of the possible effects generated by accelerated secondary electrons led to the following conclusions:

1) In terms of the velocity distributions of secondaries outside the sheath region surrounding the balloon, excitation of electromagnetic instabilities (requiring an excess momentum perpendicular to the magnetic field) is not likely to be important from an energetic point of view.

2) A phenomenon that may possibly be important and that merits further investigation is the possible excitation of UV radiation by high-energy electrons moving down the balloon flux tube and, in the absence of other inter-interactions, reaching the Earth's atmosphere. This conclusion may be drawn from a comparison of calculated power densities in energetic secondary electrons (3×10^4 ergs $cm^{-2}sec^{-1}$ for a balloon radius $R_B = 5m$) with corresponding numbers referring to the actual measurements of Lyman-α/UV excitation at the foot of the Io's flux tube.

The next topic considered is what we have called "spontaneous" wave generation, i.e., the electromagnetic disturbance that is naturally associated with the motion of TSS across Earth's magnetic field. In particular we have focussed our attention on the possible spontaneous generation of low-frequency Alfvèn waves. This requires rather large balloon dimensions ($R_B \geq 20$ meters, for motion perpendicular to B) and power levels that one gets for Alfvèn waves guided in the flux tube cut through by the balloon are significant: $P_{AW} \gtrsim 100$ watts. We have also determined the feasibility of detecting this Alfvènic disturbance on the ground, through the use of cryogenic magnetometers. As we have discussed, to have significant power in spontaneously guided Alfvèn waves, one needs large balloon dimensions. On the other hand, by modulating the natural current in the tether (through modulation of the electron gun at the Orbiter in configuration B), one would use TSS as a long antenna and then take advantage of the properties of the long tether itself as a radiator. This possibility deserves further study.

6. References

Alpert, Ya. L.; Gurevich, A.V.; and Pitaevskii, L.P. 1965. Space Physics with artificial satellites. New York: Consultant Bureau.

Anderson, M.P.; Arnold, D.A.; Colombo, G.; Dobrowolny, M.; Grossi, M.D.; and Kirschner, L.R. 1979. Orbiting tether's electrodynamic interactions. Final Report, NASA Contract NAS5-25077, April.

Arnold, D.A., and Dobrowolny, M. 1980. Transmission line model of the interaction of a long metal wire with the ionosphere. Radio Science 15: 1149-1161.

Atreya, S.K.; Yung, Y.L.; Donahu, T.M.; and Barver, E.S. 1977. Astrophysical Journal 218, L83-L87.

Banks, P. et at., 1980. Tethered Satellite System, Facility Requirements Definition Team Report, CASS, Utah State U., Logan, Utah, April.

Colombo, G. 1980. Private Communications.

Dobrowolny, M.; Colombo, G.; and Grossi, M.D. 1976. Electrodynamics of long tethers in the near-Earth environment. SAO Report in Geoastronomy No. 3, October, re-issued April 1979.

Dobrowolny, M; Arnold, D.A.; Colombo, G.; and Grossi, M.D. 1979. Mechanisms of electrodynamic interactions between a tethered satellite system and the ionosphere. SAO Reports in Radio and Geoastronomy No. 6, August.

Dobrowolny, M. 1979. Wave and particle phenomena induced by an electrodynamic tether. SAO Special Report 388, November.

Drell, S.D.; Foley, H.M.; and Ruderman, M.A. 1965. Drag and propulsion of large satellites in the ionosphere: an Alfven propulsion engine in space. Journal Geophysical Research Vol. 70, 3131-3145.

Einaudi, F., and Wait, J.R. 1971a. Analysis of the excitation of the earth-ionosphere wave guide by a satellite-borne antenna-I, Canadian Journal Physics 49 (4), 447-457.

Einaudi, F., and Wait, J.R. 1971b. Analysis of the excitation of the earth-ionosphere wave guides by a satellite-borne antenna-II. Canadian Journal Physics 49 (11), 1452-1460.

Goldreich, P., and Lynden-Bell, D. 1969. Io, a Jovian unpolar inductor. Astrophysical Journal 156, 59-78.

Grossi, M.D., and Colombo, G. 1978. Interactions of a tethered satellite system with the ionosphere. In Proceedings of the University of Alabama/ NASA Workshop in the Uses of a Tethered Satellite System, ed. by S.T. William, Huntsville, Ala.: University of Alabama, 176-181.

Gurnett, D.A. 1972. Sheath effects and related charged particle acceleration by Jupiter's satellite Io. Astrophysical Journal 175, 525-533.

Hagstrum, H.D. 1956. Physical Review, 104, 1516.

Hanson, W.B. 1965. Structure of the ionosphere. In Satellite Enviroment Handbook, ed. by F.S. Johnson Stanford, Calif.: Stanford University Press, 23-41.

Higatsherger, M.J.; Demorest, H.L.; and Nier, A.O. 1954. Journal of Applied Physics, 25, 883.

Hubbard, R.F.; Shawhan, S.D.; and Joyce, G. 1976. Io as an emitter of 100 keV electrons. Journal Geophysical Research 79, 920-928.

Jeffrey, A., and Taniuti, T. 1964. Non-linear wave propagation. New York: Academic Press.

Kelly, F.J.; Baker, D.J.; and Chayt, G.A. 1974. Spreading of waves launched by a ELF/VLF satellite. NRL Report 7814, December 31.

Kelly, F.J., Baker, D.J., and Chayt, G.A. 1976. Spreading of waves emitted by a ELF/VLF Source in the Magnetosphere, Radio Science 11, pp. 93-106.

Linson, L.M. 1969. Current-voltage characteristics of an electro-emitting satellite in the ionosphere. Journal Geophysical Research 74, 2368-2375.

Mallinckrodt, A.J., and Carlson, C.W. 1978. Relations between transverse electric fields and field aligned currents. *Journal Geophysical Research* *33*, 1426-1432.

Mangeney, A., and Veltri, P. 1976. On the theory of type I radio bursts. 1. Beam plasma instabilities in a turbulent magnetized plasma. *Astronomy and Astrophysics* *47*, 165.

Massey, H.S.W., and Burhop, E.H.S. 1952. In "Electronic and Ionic Impact Phenomena," Chapter IX, pp. 541, Publisher: Oxford at Clarendon Press.

McDaniel, E.W. 1964. Collisional phenomena in ionized paces. Chapter 13, pp. 629-649, J. Wiley & Sons Publishers.

Melrose, D.B. 1973. *Australian Journal of Physics* *26*, 229.

Ness, N.F.; Acuna, M.H.; Lepping, R.P.; Burlaga, L.F.; Behannon, K.W.; and Newbauer, F.M. 1979. Magnetic field studies at Jupiter by Voyager 1. Preliminary results. *Science* *204*, 982-987.

Newbauer, F.M. 1980. Non-linear standing Alfven wave current system at Io: theory. *Journal Geophysical Research* *85*, 1171-1178.

Pappert, R.A. 1973. Excitation of the earth-ionosphere waveguide by point dipoles at satellite heights. *Radio Science* *8*, No. 6, 535-545.

Stix, T.H. 1962. The Theory of Plasma Waves. New York: McGraw Hill.

Williamson, R.P., and Banks, P.M. 1976. The tethered balloon-current generator: A space shuttle-tethered sub-satellite for plasma studies and power generation. Final Report, NOAA Contract USDC-NOAA 03-5-022-60, January.

Whipple, E.C., Jr. 1965. The equilibrium electric potential of a body in the upper atmosphere and in interplanetary space. NASA/GSFC Document X-615-65-296.